CrossMark

JM PAPERS

Shape matters: a Brownian microswimmer in a channel

Hongfei Chen[1],† and Jean-Luc Thiffeault[1],†

[1]Department of Mathematics, University of Wisconsin – Madison, 480 Lincoln Dr., Madison, WI 53706, USA

We consider the active Brownian particle model for a two-dimensional microswimmer with fixed speed, whose direction of swimming changes according to a Brownian process. The probability density for the swimmer obeys a Fokker–Planck equation defined on the configuration space, whose structure depends on the swimmer's shape, centre of rotation and domain of swimming. We enforce zero probability flux at the boundaries of configuration space. At first neglecting hydrodynamic interactions, we derive a reduced equation for a swimmer in an infinite channel, in the limit of small rotational diffusivity, and find that the invariant density depends strongly on the swimmer's precise shape and centre of rotation. We also give a formula for the mean reversal time: the expected time taken for a swimmer to completely reverse direction in the channel. Using homogenization theory, we find an expression for the effective longitudinal diffusivity of a swimmer in the channel, and show that it is bounded by the mean reversal time. Finally, we include hydrodynamic interactions with walls, and examine the role of shape.

Key words: micro-organism dynamics

1. Introduction

Microswimmers are common in nature – they include bacteria, spermatozoa, some algae and synthetic swimmers. In almost all contexts these swimmers interact with boundaries, either biological (e.g. the gut, cell walls) or man-made (e.g. tubes, filters). These interactions have been studied experimentally, numerically and theoretically by many groups. The two main aspects of interaction are hydrodynamic (mediated by the fluid) and steric (direct contact with the boundary); they can have different relative importance depending on the context, but it is widely accepted that both can play a crucial role (Drescher *et al.* 2011; Kantsler *et al.* 2013; Contino *et al.* 2015; Bianchi, Saglimbeni & Leonardo 2017).

† Email addresses for correspondence: hchen475@wisc.edu, jeanluc@math.wisc.edu

In the present paper we will be concerned with modelling the steric interaction of a microswimmer with solid surfaces, with an emphasis on the role of the swimmer's shape. For simplicity, the swimmer will be two-dimensional with a fixed shape, although, in principle, the theory could be extended to include a deformable body or flagella. To keep the model tractable, we drop the hydrodynamic interactions when deriving theoretical results, but in § 8 we quantify their importance relative to steric interactions.

1.1. *Previous work*

Many models have been proposed to mimic the behaviour of microswimmers, with the simplest being the active Brownian particle (ABP) model (Ai *et al.* 2013; Redner, Hagan & Baskaran 2013; Stenhammar *et al.* 2014; Solon *et al.* 2015; Zöttl & Stark 2016; Wagner, Hagan & Baskaran 2017) where a particle moves with constant speed and both its swimming direction and spatial position are subject to independent diffusion processes. A more complicated model has the organism moving in a straight line for a random time (run), followed by a random change in direction (tumble); such run-and-tumble models have been investigated both theoretically and numerically (Tailleur & Cates 2009; Lambert, Liao & Austin 2010; Nash *et al.* 2010; Costanzo *et al.* 2012; Ezhilan, Pahlavan & Saintillan 2012; Lushi, Goldstein & Shelley 2012; Martens *et al.* 2012; Cates & Tailleur 2013; Koumakis, Maggi & Leonardo 2014; Lushi, Wioland & Goldstein 2014; Molaei *et al.* 2014; Elgeti & Gompper 2015; Ezhilan, Alonso-Matilla & Saintillan 2015; Elgeti & Gompper 2016; Lushi 2016; Razin *et al.* 2017; Sepúlveda & Soto 2017; Chen *et al.* 2018; Lee, Szuttor & Holm 2019). There are also more complex models that incorporate hydrodynamic effects (Fauci & McDonald 1995; Saintillan, Shaqfeh & Darve 2006*a*, *b*; Saintillan & Shelley 2007, 2008; Crowdy & Or 2010; Evans & Lauga 2010; Rusconi *et al.* 2010; Saintillan 2010; Shum, Gaffney & Smith 2010; Crowdy & Samson 2011; ten Hagen, Wittkowski & Löwen 2011; Costanzo *et al.* 2012; Obuse & Thiffeault 2012; Saintillan & Shelley 2013; Li & Ardekani 2014; Lushi *et al.* 2014; Takatori, Yan & Brady 2014; Bricard *et al.* 2015; Lushi & Vlahovska 2015; Spagnolie *et al.* 2015; ten Hagen *et al.* 2015; Yeo, Lushi & Vlahovska 2015; Mathijssen *et al.* 2016; Wioland, Lushi & Goldstein 2016; Theillard, Matilla & Saintillan 2017; Daddi-Moussa-Ider *et al.* 2018; Lushi, Goldstein & Shelley 2018; Theers *et al.* 2018; Alonso-Matilla & Saintillan 2019; Wagner, Hagan & Baskaran 2019). In the present paper we will limit ourselves to the ABP model.

Experiments with microswimmers near boundaries are also plentiful (Rothschild 1963; Frymier *et al.* 1995; Woolley 2003; DiLuzio *et al.* 2005; Lauga 2006; Hill *et al.* 2007; Berke *et al.* 2008; Li, Tam & Tanf 2008; Drescher *et al.* 2011; Volpe *et al.* 2011; Kantsler *et al.* 2013; Kim *et al.* 2014; Contino *et al.* 2015; Mok, Dunkel & Kantsler 2019). As early as 1963, Rothschild measured the density of bull spermatozoa between two glass plates and found accumulation near the plates. Accumulation as well as local alignment and preferred tail rotation were also observed in later experiments (Rothschild 1963; Woolley 2003; Lauga 2006; Hill *et al.* 2007; Berke *et al.* 2008; Li *et al.* 2008; Drescher *et al.* 2011; Li *et al.* 2011; Volpe *et al.* 2011; Denissenko *et al.* 2012; Kantsler *et al.* 2013; Lefauve & Saintillan 2014; Contino *et al.* 2015). Simulations have shown that either hydrodynamic interactions or steric interactions with thermal fluctuations can lead to accumulation. Later work found that steric effects dominate at walls, while hydrodynamic interactions can play an important role (Drescher *et al.* 2011; Kantsler *et al.* 2013; Contino *et al.* 2015; Bianchi *et al.* 2017).

In principle, the interaction of microswimmers with boundaries requires modelling of both hydrodynamic and steric interactions. Some groups use far-field approximations for hydrodynamic interactions (Katz 1974; Katz & Blake 1975; Katz, Blake & Paverifontana

1975; Hernandez-Ortiz, Stoltz & Graham 2005; Saintillan *et al.* 2006*a*; Swan & Brady 2007; Elgeti & Gompper 2009; Crowdy & Or 2010; Crowdy & Samson 2011; Obuse & Thiffeault 2012; Spagnolie & Lauga 2012; Lopez & Lauga 2014; Schaar, Zöttl & Stark 2015; Sipos *et al.* 2015; Spagnolie *et al.* 2015; ten Hagen *et al.* 2015; Kaynan & Yariv 2017; Mirzakhanloo & Alam 2018; Wagner *et al.* 2019), which can be done in several ways: either explicitly with a solution of the Stokes equation, or implicitly through a resistance or mobility matrix. Spagnolie & Lauga (2012) used a multipole expansion which in principle can be applied to any swimmer shape, and Takagi *et al.* (2014) solved the Stokes equation in the lubrication limit. Zargar, Najafi & Miri (2009) solved for the mobility matrix by restricting the swimmer to planar motion near a wall. Despite some simplifications in these models, they are fairly accurate away from boundaries and reproduce observed behaviour (Lauga & Powers 2009; Marchetti *et al.* 2013; Bechinger *et al.* 2016; Zöttl & Stark 2016). However, such models remain in general fairly complicated and available theoretical results either ignore the details of swimmers such as shape, or are swimmer dependent.

Steric interactions are often included phenomenologically, such as by using wall potential functions (van Teeffelen & Löwen 2008; Wensink & Löwen 2008; Hernandez-Ortiz, Underhill & Graham 2009; Costanzo *et al.* 2012; Kaiser, Wensink & Löwen 2012; Chilukuri, Collins & Underhill 2014; Mathijssen *et al.* 2016; Tian *et al.* 2017; Caprini & Marconi 2018; Daddi-Moussa-Ider *et al.* 2018; Sepúlveda & Soto 2018; Wagner *et al.* 2019). This approach makes it easy to add boundaries to free-space simulations and has low simulation cost. Sepúlveda & Soto (2018) used Weeks–Chandler–Anderson functions and a Gaussian potential function for deformable swimmers; they treat the effective wall force as a smooth repulsive force. Hernandez-Ortiz *et al.* (2009) used Gay–Berne functions for steric exclusion of rod-shape swimmers. These models are usually a smooth approximation to the true dynamics, whereas for rigid swimmers the steric effect is by volume exclusion. Moreover, the complicated potential functions make it hard to obtain predictive formulas, although some authors used a simple harmonic potential to represent an elastic boundary, which made the problem tractable (Drescher *et al.* 2011; Nikola *et al.* 2016; Caprini & Marconi 2018).

Another way to model steric interactions is to assign a specific dynamics near the boundary such as reflecting (Li & Tang 2009; Koumakis *et al.* 2014; Volpe, Gigan & Volpe 2014; Paksa *et al.* 2016; Chen *et al.* 2018) or vanishing velocity (Sepúlveda & Soto 2018) boundary conditions, or a repulsive force condition (Spagnolie & Lauga 2012). Ezhilan & Saintillan (2015) observed that reflecting boundary conditions do not recover the behaviour observed in experiments. Other groups did not try to prescribe any specific law for swimmers at a boundary and focused on statistics such as the invariant density of swimmers (Ezhilan *et al.* 2012; Yariv & Schnitzer 2014; Yan & Brady 2015; Malgaretti & Stark 2017) and swim pressure (Caprini & Marconi 2018; Chen *et al.* 2018; Yan & Brady 2015; Speck 2020).

When modelling a collection of stochastic swimmers or the statistics of a single swimmer, an ideal approach to include steric interactions is to use no-flux boundary conditions that prevent the organism's body from entering the wall, as described by Nitsche & Brenner (1990) for passive particles. Most work in the literature using these boundary conditions assumes that swimmers have negligible size or are of spherical shape, so that they can rotate freely at a wall (Burada *et al.* 2009; Bearon, Hazel & Thorn 2011; Bruna & Chapman 2013; Yariv & Schnitzer 2014; Ezhilan & Saintillan 2015; Yan & Brady 2015; Alonso-Matilla, Ezhilan & Saintillan 2016; Malgaretti & Stark 2017; Alonso-Matilla & Saintillan 2019). Lee (2013) attempted to solve for the invariant density without spatial diffusion for point swimmers in a channel, and managed to find a solution

when swimmers had only six swimming directions. Wagner *et al.* (2017) continued Lee's work and found the invariant density for continuous swimming directions by introducing a wall density function. Schaar *et al.* (2015) later calculated the trapping time at a wall. Ai *et al.* (2013) predicted for point swimmers the optimal swimming speed, the spatial diffusion and the strength of wall potentials for maximal effective diffusion. For spherical or point swimmers, Elgeti & Gompper (2013) and Ezhilan & Saintillan (2015) investigated asymptotic solutions to the Fokker–Planck equation associated with the ABP model. Elgeti & Gompper (2016) subsequently found the invariant density for run-and-tumble spherical swimmers.

1.2. *The role of shape*

The admissible positions and orientations of a non-spherical swimmer are constrained by the presence of walls; the set of admissible values of the degrees of freedom is the configuration space (Nitsche & Brenner 1990) (see § 2). A natural way to include the shape of a swimmer into a model is thus to impose no-flux boundary conditions on the configuration space itself. Krochak, Olson & Martinez (2010) and Ezhilan & Saintillan (2015) used steric exclusion with no-flux boundary conditions for rigid fibres and rod-like swimmers, respectively, and simulated the invariant density in a channel in the presence of flow.

In the present paper we propose a framework to incorporate the shape of a swimmer into the boundary conditions of a partial differential equation describing its dynamics. The partial differential equation (PDE) is the Fokker–Planck equation derived from the two-dimensional ABP model with no-flux boundary conditions in configuration space. For simplicity, we ignore hydrodynamic interactions for now. (We will introduce them in § 8.) The configuration space is determined by the swimmer's shape and the domain of swimming, which we take to be an infinite channel. We solve explicitly for the invariant density in the limit of small rotational diffusivity. In the same limit, we also solve for the mean reversal time and the longitudinal effective diffusivity of the swimmer. All these quantities are greatly influenced by the shape of the swimmer. In particular the effective diffusivity can become very large when the swimmer tends to align parallel to the channel walls, which can surprisingly occur even for circular swimmers when their centre of rotation does not coincide with the geometric centre (see below). In § 8, we add hydrodynamic interactions into the ABP model, and examine how the cross-sectional invariant density varies with the shape-dependent configuration space.

In the literature so far, authors have often prevented swimmers from entering inside boundaries by applying some *ad hoc* repulsive force or potential, which models steric interactions. Our main point is that a similar effect can be achieved by a no-flux boundary condition, which is natural in the context of a Fokker–Planck equation. It has the advantage of naturally involving the shape of the organism through the configuration space. As we will, this mathematical elegance allows analytical progress for simple swimmer shapes, at least when neglecting hydrodynamic interactions as a first approximation.

An important observation is in order regarding the ABP model for a finite-size swimmer. The ABP model implicitly assumes that the swimmer rotates about some distinguished fixed point in a co-moving frame. The precise location of this point becomes important when the swimmer has finite size and boundaries are present. For example, figure 1 shows an elliptical swimmer approaching a boundary: the direction of swimming is given by the angle θ, which is measured counterclockwise from the horizontal, so that $\theta < 0$ corresponds to swimming towards the wall. The angle θ is measured around a point we call the centre of rotation of the swimmer. For a free particle, this corresponds to the
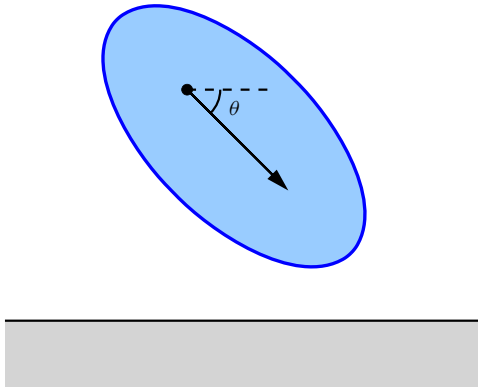
Figure 1. An elliptical swimmer approaching a wall at a direction $\theta = -\pi/4$. The centre of rotation is not necessarily the geometric centre of the ellipse.

centre of hydrodynamic reaction defined by Happel & Brenner (1983, p. 174). For an ellipse it would coincide with the geometrical centre. However, the swimmer's propulsion mechanism (e.g. flagella), which is abstracted here since we consider fixed shapes, can displace this centre. Hence, we treat the centre of rotation as a parameter that may be adjusted to model a particular swimmer. To parallel terminology based on the type of propulsion used by a microorganism (Hernandez-Ortiz *et al.* 2005; Saintillan & Shelley 2007; Hernandez-Ortiz *et al.* 2009; Saintillan & Shelley 2011), when the centre of rotation is ahead of the geometric centre we will call the swimmer front rotating; when it is behind we call it rear rotating. We assume the centre of rotation is inside a swimmer's body. If the swimmer does not interact with boundaries, then the centre of rotation is not particularly important to the dynamics; but with external boundaries it can influence the tendency of the swimmer to align parallel or perpendicular to a wall, depending on its shape (Lushi, Kantsler & Goldstein 2017). In fact, we will see that even a circular particle can align with a wall if its centre of rotation is behind the geometric centre, despite the absence of hydrodynamic interactions.

1.3. *Outline*

In this paper we focus exclusively on a two-dimensional swimmer undergoing steric interactions. In § 2 we describe the configuration space for a swimmer with an arbitrary fixed convex shape, in particular when the swimmer is confined to a channel consisting of two infinite parallel walls. A crucial quantity is the wall distance function, which describes the swimmer's closest point of approach to a wall as a function of the swimmer's orientation. We give explicit examples for needle (rod-like), elliptical, and teardrop-shaped swimmers. The wall distance function can then be used twice to determine the full configuration space in a channel. This configuration space is open if the swimmer can reverse direction in the channel, or closed if the channel is too narrow to do so. We also describe symmetries of the configuration space that follow from symmetries of the swimmer and channel, the most important being the case where a swimmer is left–right symmetric.

In § 3 we describe the stochastic ABP model for our swimmer, and give its corresponding Fokker–Planck equation. This leads to the natural no-flux boundary conditions that we impose at the solid walls. For the infinite channel geometry we

average over the lengthwise coordinate. In §4 we simplify the model by assuming a small rotational diffusivity. This leads to a reduced equation, which is a partial differential equation in one time variable and one angle. The configuration geometry is completely encoded into a single effective angular drift function.

In §5 we solve for the steady state of the reduced equation, which gives us the invariant probability density of the swimmer, or invariant density for short. The invariant density is strongly dependent on the shape and centre of rotation, as we show with some explicit examples, typically in the limit of rapid swimming. In particular, we show that circular swimmers can align either parallel or perpendicular to the walls, depending on whether they are rear or front rotating, respectively. When a swimmer has broken left–right symmetry, it can undergo a net rotation due to repeated biased interactions with the walls.

We introduce the mean reversal time (MRT) of a swimmer in §6: the expected time for a swimmer to fully reverse direction in an open channel. This is a generalization of the turnaround time of Holcman & Schuss (2014), who described the expected time for a Brownian needle to reverse direction when its length is slightly shorter than the channel width. For a left–right symmetric swimmer we give a simple integral formula for the MRT. We explicitly compute the MRT in some limits, in particular for a fast swimmer. The MRT in this fast case is exponentially long, since the swimmer sticks to a wall for a very long time before undergoing a large enough random fluctuation that causes reversal.

In §7 we use a homogenization theory approach to find the longitudinal effective diffusivity D_{eff} for the swimmer in an open channel. In the same reduced limit as above (small rotational diffusion) we give an integral formula for the diffusivity. For a fast swimmer we might expect that the effective diffusivity is related to the MRT: the swimmer makes large excursions and sometimes reverses direction, thereby undergoing an effective random walk for long times. Indeed, we obtain the rigorous bound

$$D_{eff} \le D_X + \tfrac{1}{2}\tau_{rev}\, U^2, \tag{1.1}$$

where D_X is the diffusivity of the swimmer along the direction of swimming, τ_{rev} is the MRT and U is the swimming speed. The term $\tfrac{1}{2}(\tau_{rev}\, U)^2/\tau_{rev}$ is equal to the diffusivity for an unbiased random walk with step size $\tau_{rev}U$ and step time τ_{rev}.

In §8, we incorporate hydrodynamic interactions of the swimmer with walls, using the same interaction terms as in Spagnolie *et al.* (2015). We compare the cross-sectional invariant density in a narrow channel for a configuration space corresponding to an ellipsoidal and a near-spherical shape. Finally, we offer some concluding remarks in §9.

2. Configuration space

In this section we describe how the swimmer's shape interacts with boundaries to create configuration space. We first establish coordinate systems for a convex swimmer (§2.1): the fixed laboratory frame and a frame rotating with the swimmer. These are both necessary since the direction of swimming and the magnitude of diffusion are tied to the swimmer's shape, and may be different along different axes (§3). We use the term 'swimmer' throughout, but our entire formalism applies to passive particles as well, for which $U = 0$. We consider an arbitrary contact point between a swimmer's body and a single wall, and show how to derive the wall distance function for the swimmer. We present a few examples: a needle (one-dimensional segment), an ellipse and a 'teardrop' shape. These are all swimmers with a left–right axis of symmetry, but our formalism applies to more general swimmers as well.
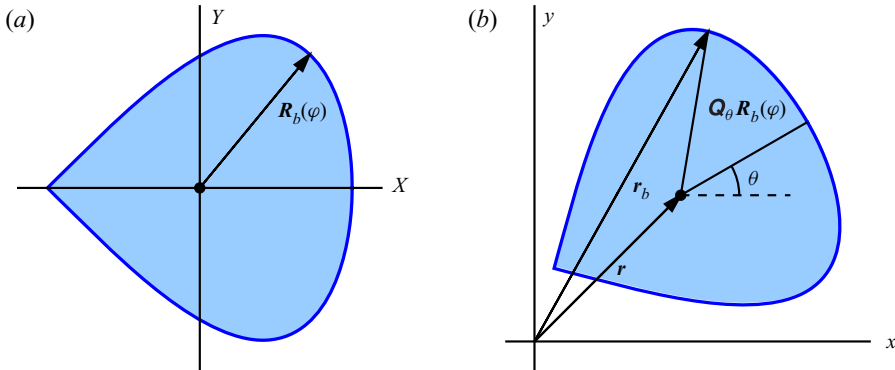
Figure 2. Boundary of a convex swimmer in (*a*) the swimmer's frame, with the swimming direction along the positive X axis, and (*b*) the fixed laboratory frame, where the swimming direction makes an angle θ with the x axis.

In § 2.2 we use the wall distance function to obtain the configuration space for a swimmer confined between two infinite, parallel walls. Two very different cases emerge: in the open channel configuration the channel is wide enough to allow the swimmer to completely reverse direction, whereas in the closed configuration the swimmer is unable to do so.

2.1. *The wall distance function*

The shape of a swimmer is expressed by giving its boundary in parametric form

$$\boldsymbol{R} = \boldsymbol{R}_b(\varphi) = (X_b(\varphi), Y_b(\varphi)), \quad -\pi < \varphi \leq \pi, \tag{2.1}$$

where $\boldsymbol{R}_b(\varphi)$ is a 2π-periodic, piecewise-smooth function (figure 2a). By convention, the swimming direction $\boldsymbol{R}_b(0)$ is along the positive X axis in the swimmer's co-moving and co-rotating frame. The origin of the $\boldsymbol{R} = (X, Y)$ coordinate system is the centre of rotation of the swimmer. Note that we do not require $\tan \varphi = Y_b(\varphi)/X_b(\varphi)$, that is, φ does not necessarily correspond to the polar angle of $\boldsymbol{R}_b(\varphi)$.

In a fixed (laboratory) frame, the boundary of the swimmer is located at (figure 2b)

$$(x_b, y_b) = \boldsymbol{r}_b(\theta, \varphi) = \boldsymbol{r} + \boldsymbol{Q}_\theta \cdot \boldsymbol{R}_b(\varphi), \quad -\pi < \varphi, \theta \leq \pi, \tag{2.2}$$

where $\boldsymbol{r} = (x, y)$ denotes the centre of rotation of the swimmer and

$$\boldsymbol{Q}_\theta = \begin{pmatrix} \cos \theta & -\sin \theta \\ \sin \theta & \cos \theta \end{pmatrix} \tag{2.3}$$

is a rotation matrix.

Now take the swimmer to be touching an infinite wall along $y = 0$, as shown in figure 3(*a*). The contact point W between the swimmer and the wall has coordinates

$$(x_b, 0) = \boldsymbol{r} + \boldsymbol{Q}_\theta \cdot \boldsymbol{R}_b(\varphi). \tag{2.4}$$

We wish to solve for the swimmer's centre of rotation $\boldsymbol{r} = (x, y)$, which depends only on the convex hull of the swimmer; hence, the swimmer's shape may be assumed convex without loss of generality. We proceed differently depending on whether the contact point W is a corner or a smooth boundary point. (Note that the analysis below can be couched in the language of Legendre transformations and convex analysis, but we opt here for a direct treatment.)
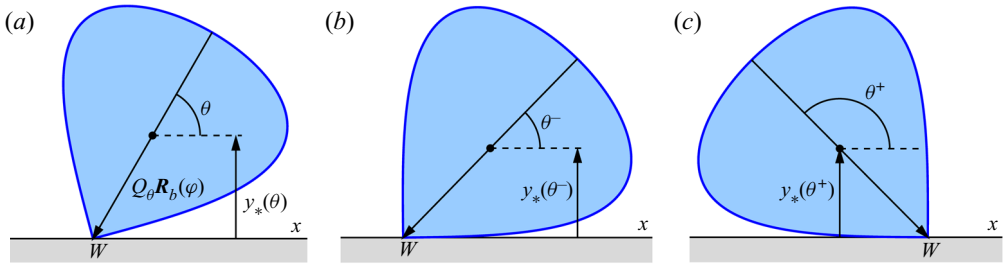
Figure 3. (*a*) Convex swimmer touching a horizontal wall at a corner point W. (*b,c*) Holding W fixed, the angle θ can vary from the right-tangency angle θ^- to the left-tangency angle θ^+.

2.1.1. *Corner*

Consider first the case where the contact point W corresponds to a corner of the piecewise-smooth boundary, as in figure 3(*a*). The parameter φ has a fixed value for corner W. The allowable range of θ is then determined by the right- and left-tangency values of θ

$$\theta^- \leq \theta \leq \theta^+, \quad \tan\theta^\pm = -Y_b'(\varphi^\pm)/X_b'(\varphi^\pm), \tag{2.5}$$

as depicted in figures 3(*b*) and 3(*c*). Here, Y_b' and X_b' are derivatives of Y_b and X_b.

For this range of θ, we can then use (2.4) to deduce the range of y values

$$y_*(\theta) = -\sin\theta X_b(\varphi) - \cos\theta Y_b(\varphi), \quad \theta^- \leq \theta \leq \theta^+. \tag{2.6}$$

We call y_* the wall distance function. It characterizes the minimum distance from the swimmer's centre of rotation to a horizontal wall, as a function of the swimmer's orientation. Observe that a given corner corresponds to a single φ value, but a range of θ values.

EXAMPLE 2.1 (needle swimmer). *As a simple example, take*

$$X_b(\varphi) = \tfrac{1}{2}\ell\cos\varphi - X_{rot}, \quad Y_b(\varphi) = 0. \tag{2.7}$$

This is the needle swimmer with centre of rotation displaced by X_{rot}, with $|X_{rot}| \leq \ell/2$. It consists of a one-dimensional segment of length ℓ, with degenerate 'corners' at $\varphi_1 = 0$ and $\varphi_2 = \pi$. At $\varphi = \varphi_1 = 0$, we have $-\pi \leq \theta \leq 0$, so from (2.6) $y_*(\theta) = -\sin\theta X_b(\varphi_1) = -\sin\theta(\tfrac{1}{2}\ell - X_{rot})$. At $\varphi = \varphi_2 = \pi$, we have $0 \leq \theta \leq \pi$, so from (2.6) $y_*(\theta) = -\sin\theta X_b(\varphi_2) = -\sin\theta(-\tfrac{1}{2}\ell - X_{rot})$. We can combine these cases by writing

$$y_*(\theta) = \tfrac{1}{2}\ell|\sin\theta| + X_{rot}\sin\theta, \quad -\pi < \theta \leq \pi. \tag{2.8}$$

Only needle positions with $y \geq y_*(\theta)$ are allowed; see figures 4(a) and 4(b) for a plot. For the case $X_{rot} = 0$, this type of swimmer and configuration space was investigated by Ezhilan & Saintillan (2015).

We will typically use ℓ to denote the maximum diameter of a swimmer, which controls whether or not it can reverse direction for a given channel width (§ 2.2). The parameter X_{rot} controls the position of the centre of rotation: for $X_{rot} > 0$ it is closer to the front, and for $X_{rot} < 0$ it is towards the rear. We refer to these cases as front rotating and rear rotating, respectively.
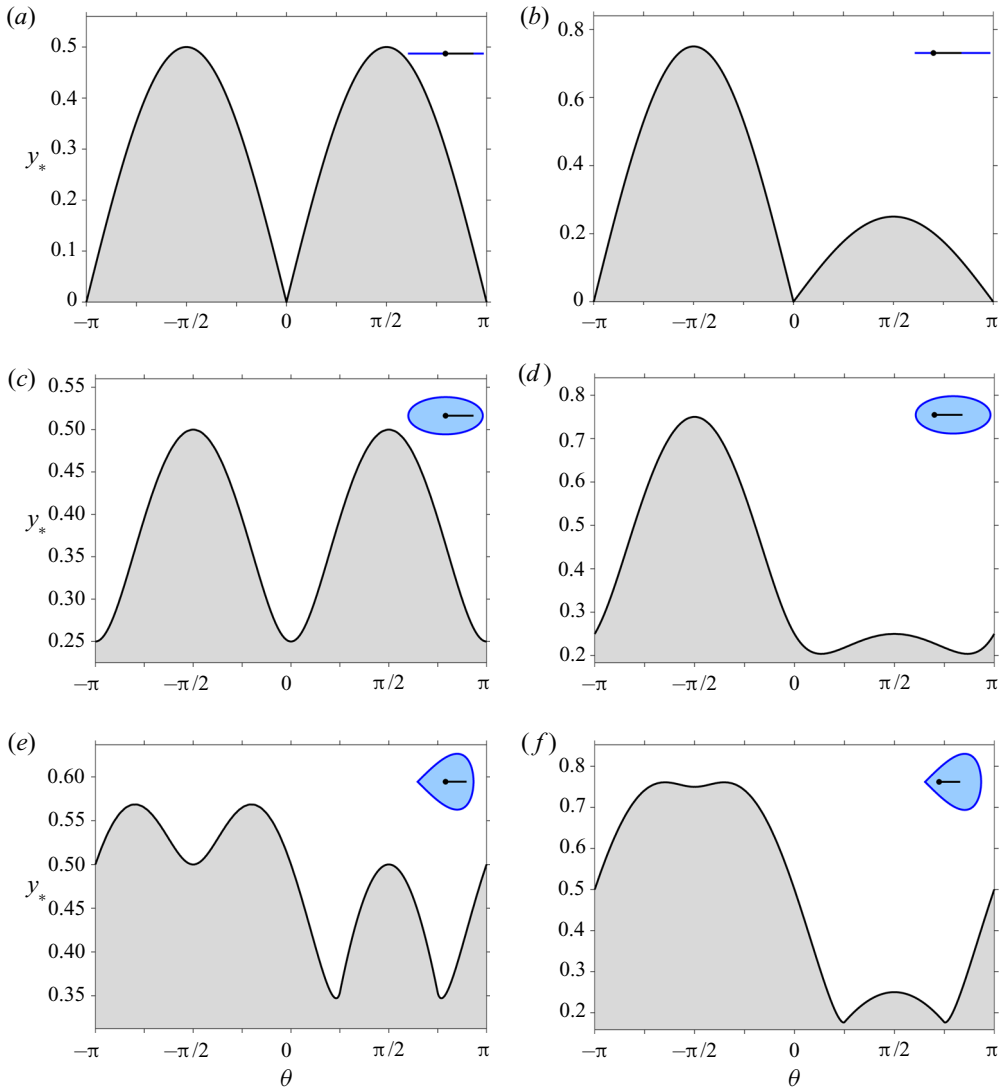
916 A15-8

Figure 4. The wall distance function $y_*(\theta)$ for three different swimmers: (*a,b*) needle of length $\ell = 2a = 1$; (*c,d*) ellipse of length $\ell = 2a = 1$ and width $2b = 1/2$; (*e, f*) teardrop-shaped swimmer of size 1 by 1. The inset shows the swimmer shape and centre of rotation, with swimming direction to the right. The right column has centre of rotation displaced to $X_{rot} = -1/4$.

2.1.2. *Smooth boundary point*

When the contact point W is at a smooth boundary point, given θ we wish to solve for (x, y) and φ. Two equations come from (2.4), but we need a third, which stems from requiring that the tangent to the swimmer,

$$\boldsymbol{t}_b = \partial_\varphi \boldsymbol{r}_b = \boldsymbol{Q}_\theta \cdot \boldsymbol{R}'_b(\varphi), \tag{2.9}$$

is horizontal at W

$$X'_b(\varphi) \sin\theta + Y'_b(\varphi) \cos\theta = 0, \tag{2.10}$$

916 A15-9

or

$$Y_b'(\varphi)/X_b'(\varphi) = -\tan\theta. \tag{2.11}$$

We can solve (2.11) for $\varphi = \varphi_*(\theta)$, which we then use in (2.4) to obtain $r = r_*(\theta)$ at the contact point

$$r_*(\theta) = (x_*(\theta), y_*(\theta)) = -Q_\theta \cdot R_b(\varphi_*(\theta)). \tag{2.12}$$

Equation (2.11) can have more than one solution, but we keep the one that leads to a non-negative wall distance function,

$$y_*(\theta) = -\sin\theta\, X_b(\varphi_*(\theta)) - \cos\theta\, Y_b(\varphi_*(\theta)) \geq 0. \tag{2.13}$$

EXAMPLE 2.2 (elliptical swimmer). *An ellipse-shaped swimmer with semi-axes a and b can be parameterized as*

$$X_b(\varphi) = a\cos\varphi - X_{rot}, \quad Y_b(\varphi) = b\sin\varphi \tag{2.14}$$

with $|X_{rot}| \leq a$. Here, a and b are the semi-axes along and perpendicular to the swimming direction, respectively. The tangency condition (2.11) is then $\cot\varphi_*(\theta) = (a/b)\tan\theta$. After inserting in (2.13) and selecting the non-negative solution we obtain

$$y_*(\theta) = \sqrt{a^2\sin^2\theta + b^2\cos^2\theta} + X_{rot}\,\sin\theta. \tag{2.15}$$

This wall distance function is plotted in figures 4(c) and 4(d).

For $a \geq b$, it is convenient to rewrite (2.15) as

$$y_*(\theta) = a\sqrt{1 - e^2\cos^2\theta} + X_{rot}\,\sin\theta, \quad e := \sqrt{1 - b^2/a^2} < 1, \tag{2.16}$$

where e is the eccentricity. For $b = 0$ ($e = 1$) we recover the needle case (2.8), with $a = \ell/2$. The case $e = 0$ is a circular swimmer, which for $X_{rot} = 0$ has the same dynamics in our model as a point swimmer (Elgeti & Gompper 2013; Lee 2013). Note, however, that for $X_{rot} \neq 0$ even a circular swimmer can exhibit alignment with the walls (see example 5.2).

2.1.3. *General shapes*

The convex hull for a general swimmer will consist of a combination of smooth parts separated by corners, as for the 'teardrop' swimmer depicted in figure 2. The wall distance function $y_*(\theta)$ cannot be found analytically in general, but is easy to compute numerically. The simplest approach is to discretize the convex hull as a polygon, and then apply the formulas in § 2.1.1 to every corner.

EXAMPLE 2.3 (teardrop swimmer). *The 'teardrop' swimmer depicted in figure 2 is parameterized by*

$$X_b(\varphi) = a\,(2|\cos(\varphi/2)| - 1) - X_{rot}, \quad Y_b(\varphi) = b\sin\varphi, \tag{2.17}$$

with $|X_{rot}| \leq a$. This shape has a smooth boundary except for one corner at $\varphi = \varphi_1 = \pi$. The wall distance function can be obtained analytically but is a bit cumbersome; we plot it in figures 4(e) and 4(f). Unlike the previous examples, the wall distance function for the teardrop swimmer has a local minimum at $\theta = -\pi/2$, rather than a maximum. This value of θ corresponds to swimming towards the wall, and the minimum suggests that this shape has a tendency to align perpendicular to the wall, rather than parallel.

(This is similar to the triangular swimmer in Lushi et al. 2017.) In the presence of diffusion, the depth of the local minimum is a measure of how long a swimmer gets stuck in that position before fluctuating out. See also example 5.2 for another, simpler model swimmer that aligns perpendicular to the wall.

All the examples discussed thus far involve left–right-symmetric swimmers, which satisfy $(X_b(\varphi), Y_b(\varphi)) = (X_b(-\varphi), -Y_b(-\varphi))$. For this class of swimmers, the wall distance function has the symmetry

$$y_*(\theta) = y_*(\pi - \theta), \tag{2.18}$$

which is evident in figure 4.

2.2. *Channel geometry*

So far we have considered a two-dimensional swimmer above a single infinite horizontal wall. In a channel geometry, the swimmer is confined between two parallel infinite walls, at $y = \pm L/2$. Luckily, we do not need to derive a separate wall distance function for the top wall: we can deduce it by symmetry. The centre of rotation of a swimmer with wall distance function $y_*(\theta)$ will have its y coordinate in the range

$$\zeta_-(\theta) \le y \le \zeta_+(\theta), \tag{2.19}$$

where

$$\zeta_-(\theta) = y_*(\theta) - L/2, \quad \zeta_+(\theta) = -y_*(\theta + \pi) + L/2. \tag{2.20}$$

This means that $\zeta_\pm$ are related by the channel symmetry

$$\zeta_+(\theta) = -\zeta_-(\theta + \pi). \tag{2.21}$$

The x coordinate of the centre of rotation is unconstrained and can be any real number, but the domain for the swimming angle θ can either be $[-\pi, \pi]$ or a union of disjoint intervals. This depends on whether $\zeta_-(\theta) < \zeta_+(\theta)$ for all $\theta \in [-\pi, \pi]$, or $\zeta_+(\theta) = \zeta_-(\theta)$ for some θ. We call these two cases the open channel and the closed channel, respectively.

2.2.1. *Open channel*
In the simplest case, we have

$$\theta \in [-\pi, \pi], \quad \zeta_-(\theta) < \zeta_+(\theta). \tag{2.22}$$

In this case the swimmer can fully reverse direction in the channel. The full configuration space for the swimmer's centre of rotation is then

$$\Omega = \{(x, y, \theta) : x \in \mathbb{R}, \ \zeta_-(\theta) \le y \le \zeta_+(\theta), \ -\pi \le \theta \le \pi\} \tag{2.23}$$

periodic in the θ direction. A typical example for this configuration space is depicted in figure 5(*a*).
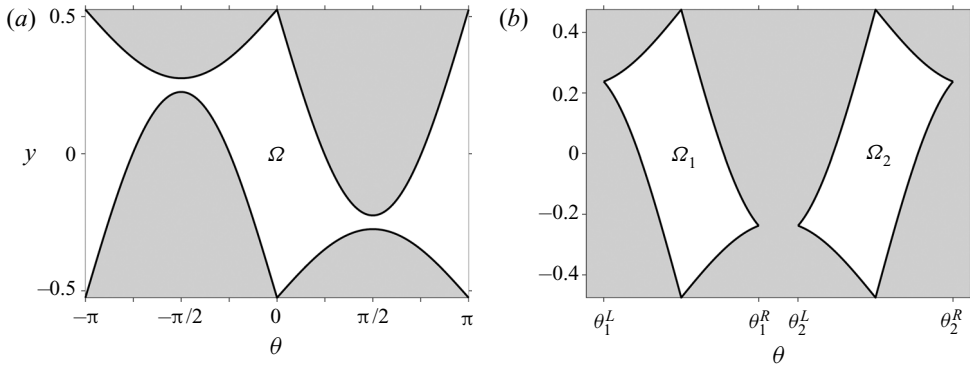
Figure 5. Configuration space for the needle in figure 4(b) of length $\ell = 2a = 1$ in (a) an open channel of width $L = 1.05$; (b) a closed channel of width $L = 0.95$. (x direction not shown.)

2.2.2. *Closed channel*

Another possibility is that $\zeta_+(\theta_i) = \zeta_-(\theta_i)$ for some set of points $\{\theta_i\}$. This breaks up $[-\pi, \pi]$ into inadmissible intervals where $\zeta_-(\theta) > \zeta_+(\theta)$, and N disjoint admissible intervals

$$\theta \in (\theta_i^L, \theta_i^R), \quad \text{with } \zeta_-(\theta) < \zeta_+(\theta), \quad i = 1, \ldots, N. \tag{2.24}$$

The relevant interval is determined by the initial orientation of the swimmer. The motion of the swimmer then takes place in the configuration space

$$\Omega_i = \{(x, y, \theta) : x \in \mathbb{R}, \ \zeta_-(\theta) \le y \le \zeta_+(\theta), \ \theta_i^L \le \theta \le \theta_i^R\}, \tag{2.25}$$

which is not periodic in the θ direction. A typical example for this configuration space is depicted in figure 5(b). Note that the condition $\zeta_+(\theta_i) = \zeta_-(\theta_i)$ together with the channel symmetry (2.21) implies that $\zeta_+(\theta_i + \pi) = \zeta_-(\theta_i + \pi)$.

3. Stochastic model

Now that we have established that the domain of motion for our swimmer is described by the configuration space of § 2, we describe the stochastic model for the swimmer's motion, the ABP model. For simplicity, we neglect hydrodynamic interactions; we will include them in § 8.

3.1. *Derivation from the stochastic differential equation*

In the ABP model, the Brownian swimmer obeys the stochastic equation

$$dX = U dt + \sqrt{2D_X} \, dW_1, \tag{3.1a}$$

$$dY = \sqrt{2D_Y} \, dW_2, \tag{3.1b}$$

$$d\theta = \sqrt{2D_\theta} \, dW_3, \tag{3.1c}$$

in its own rotating reference frame. (We omitted any intrinsic swimmer rotation for simplicity, though this would not change the derivation appreciably. We will see that a net rotation can still emerge when the swimmer is not left–right symmetric.) In terms of

916 A15-12

absolute x and y coordinates, this becomes an Itô stochastic equation

$$dx = \left(U dt + \sqrt{2D_X} \, dW_1 \right) \cos \theta - \sin \theta \sqrt{2D_Y} \, dW_2, \qquad (3.2a)$$

$$dy = \left(U dt + \sqrt{2D_X} \, dW_1 \right) \sin \theta + \cos \theta \sqrt{2D_Y} \, dW_2, \qquad (3.2b)$$

$$d\theta = \sqrt{2D_\theta} \, dW_3. \qquad (3.2c)$$

For now we take U, D_X, D_Y and D_θ to be general functions of (x, y, θ, t). The corresponding Fokker–Planck equation for the probability density $p(x, y, \theta, t)$ is then

$$\partial_t p = -\nabla \cdot (Up - \nabla \cdot (\boldsymbol{D} p)) + \partial_\theta^2 (D_\theta \, p), \qquad (3.3)$$

where $\nabla := \hat{\boldsymbol{x}} \, \partial_x + \hat{\boldsymbol{y}} \, \partial_y$, and the drift vector and diffusion tensor are respectively

$$U = \begin{pmatrix} U \cos \theta \\ U \sin \theta \end{pmatrix}, \quad \boldsymbol{D} = \begin{pmatrix} D_X \cos^2 \theta + D_Y \sin^2 \theta & \frac{1}{2}(D_X - D_Y) \sin 2\theta \\ \frac{1}{2}(D_X - D_Y) \sin 2\theta & D_X \sin^2 \theta + D_Y \cos^2 \theta \end{pmatrix}. \qquad (3.4)$$

See Kurzthaler, Leitmann & Franosch (2016) and Kurzthaler & Franosch (2017) for the intermediate scattering function for (3.3) in the absence of boundaries and with constant parameters.

For any fixed volume V we have

$$\partial_t \int_V p \, dV = -\int_V \left(\nabla \cdot (Up - \nabla \cdot (\boldsymbol{D} p)) - \partial_\theta^2 (D_\theta \, p) \right) dV = -\int_{\partial V} \boldsymbol{f} \cdot d\boldsymbol{S}, \qquad (3.5)$$

where ∂V is the boundary of V, and the flux vector is

$$\boldsymbol{f} = Up - \nabla \cdot (\boldsymbol{D} p) - \hat{\boldsymbol{\theta}} \, \partial_\theta (D_\theta \, p). \qquad (3.6)$$

Thus, on the impermeable parts of the boundary we require the no-flux condition

$$\boldsymbol{f} \cdot \boldsymbol{n} = 0, \quad \text{on } \partial V, \qquad (3.7)$$

where $\boldsymbol{n}$ is normal to the boundary.

3.2. *Infinite channel geometry*

The previous section applies to any geometry and general U, $\boldsymbol{D}$, and D_θ, which can be functions of (x, y, θ, t). For our problem, these only depend on θ. In an infinite channel geometry (§ 2.2), which we consider in this paper, we can eliminate the along-channel direction x by defining the marginal probability density

$$\bar{p}(y, \theta, t) = \int_{-\infty}^{\infty} p(x, y, \theta, t) \, dx. \qquad (3.8)$$

In order for $\bar{p}$ to be finite, p has to decay fast enough as $|x| \to \infty$; we use this assumption to discard some terms after we integrate (3.3) from $x = -\infty$ to ∞, and find an equation for $\bar{p}$

$$\partial_t \bar{p} = -\partial_y (U \sin \theta \, \bar{p}) + \partial_y^2 \left(D_{yy} \bar{p} \right) + \partial_\theta^2 \left(D_\theta \, \bar{p} \right), \qquad (3.9)$$

where from (3.4) $D_{yy} = [\boldsymbol{D}]_{22} = D_X \sin^2 \theta + D_Y \cos^2 \theta$. For the rest of the paper we take U, D_X, D_Y and D_θ to be constants, so that (3.9) simplifies to

$$\partial_t \bar{p} = -U \sin \theta \, \partial_y \bar{p} + D_{yy}(\theta) \, \partial_y^2 \bar{p} + D_\theta \, \partial_\theta^2 \bar{p}. \qquad (3.10)$$

(Note that, instead of defining $\bar{p}$ as in (3.8), we could assume that p is independent of x, in which case p is a density per unit length that satisfies (3.10).) Equation (3.10) is our

main focus. The corresponding flux vector (3.6) reduces to

$$\bar{\boldsymbol{f}} = (U \sin\theta\, \bar{p} - D_{yy}(\theta)\, \partial_y\bar{p})\, \hat{\boldsymbol{y}} - D_\theta\, \partial_\theta\bar{p}\, \hat{\boldsymbol{\theta}}. \tag{3.11}$$

For the channel geometry, the domain can be characterized by $\zeta_-(\theta) < y < \zeta_+(\theta)$, so the normal vector is

$$\bar{\boldsymbol{n}} = \zeta'_\pm(\theta)\, \hat{\boldsymbol{\theta}} - \hat{\boldsymbol{y}}. \tag{3.12}$$

The no-flux boundary conditions on (3.10) comes from (3.7)

$$\bar{\boldsymbol{f}} \cdot \bar{\boldsymbol{n}} = -(U \sin\theta\, \bar{p} - D_{yy}(\theta)\, \partial_y\bar{p}) - \zeta'_\pm(\theta)\, D_\theta\, \partial_\theta\bar{p} = 0, \quad y = \zeta_\pm(\theta). \tag{3.13}$$

For convenience, we gather together the main (3.10) and its no-flux boundary condition (3.13) for an infinite channel geometry

$$\partial_t\bar{p} + U \sin\theta\, \partial_y\bar{p} - D_{yy}(\theta)\, \partial_y^2\bar{p} - D_\theta\, \partial_\theta^2\bar{p} = 0, \quad \zeta_-(\theta) < y < \zeta_+(\theta), \tag{3.14a}$$

$$U \sin\theta\, \bar{p} - D_{yy}(\theta)\, \partial_y\bar{p} + \zeta'_\pm(\theta)\, D_\theta\, \partial_\theta\bar{p} = 0, \quad y = \zeta_\pm(\theta). \tag{3.14b}$$

As discussed in §2, the domain in θ is $[-\pi, \pi]$ (periodic) for $\zeta_-(\theta) < \zeta_+(\theta)$, which means the swimmer can fully reverse direction in the channel (open-channel configuration, figure 5a). If $\zeta_-(\theta) \le \zeta_+(\theta)$, the domain 'pinches off' whenever $\zeta_-(\theta) = \zeta_+(\theta)$, and consists of two or more disconnected pieces (closed-channel configuration, figure 5b).

4. Reduced equation

Equation (3.14) is a challenging equation to solve, in particular because of the complicated boundary shape. We can dramatically simplify the problem by assuming that the diffusivity D_θ is small, and carrying out an expansion in powers of $\varepsilon = D_\theta$. We call this the small-D_θ or reduced limit. The reduced form of (3.14), given by (4.17), will enable us to solve for the invariant density for a swimmer in §5, as well as many other quantities of interest such as a swimmer's mean reversal time (§6) and its effective diffusivity along the channel (§7).

Take (3.14) and write $D_\theta = \varepsilon$:

$$U \sin\theta\, \partial_y\bar{p} - D_{yy}(\theta)\, \partial_y^2\bar{p} = \varepsilon\, (\partial_\theta^2\bar{p} - \partial_T\bar{p}), \quad \zeta_-(\theta) < y < \zeta_+(\theta), \tag{4.1a}$$

$$U \sin\theta\, \bar{p} - D_{yy}(\theta)\, \partial_y\bar{p} = -\varepsilon\, \zeta'_\pm(\theta)\, \partial_\theta\bar{p}, \quad y = \zeta_\pm(\theta), \tag{4.1b}$$

where we also defined a slow time $T = \varepsilon t$, $\partial_t \to \varepsilon\, \partial_T$. We write the regular expansion

$$\bar{p}(\theta, y, T) = \bar{p}_0(\theta, y, T) + \varepsilon\, \bar{p}_1(\theta, y, T) + \varepsilon^2\, \bar{p}_2(\theta, y, T) + \dots, \tag{4.2}$$

and proceed to solve for $\bar{p}_i$ order by order.

At order ε^0, (4.1) is

$$U \sin\theta\, \partial_y\bar{p}_0 - D_{yy}(\theta)\, \partial_y^2\bar{p}_0 = 0, \quad U \sin\theta\, \bar{p}_0 - D_{yy}(\theta)\, \partial_y\bar{p}_0 = 0, \quad y = \zeta_\pm(\theta) \tag{4.3}$$

with solution

$$\bar{p}_0(\theta, y) = Q(\theta, T)\, e^{\sigma(\theta) y}, \quad \sigma(\theta) := U \sin\theta / D_{yy}(\theta), \tag{4.4}$$

where $Q(\theta, T)$ is as-yet undetermined.

At order ε^1, (4.1) is

$$U \sin\theta \, \partial_y \bar{p}_1 - D_{yy}(\theta) \, \partial_y^2 \bar{p}_1 = \partial_\theta^2 \bar{p}_0 - \partial_T \bar{p}_0, \tag{4.5a}$$

$$U \sin\theta \, \bar{p}_1 - D_{yy}(\theta) \, \partial_y \bar{p}_1 = -\zeta'_\pm(\theta) \, \partial_\theta \bar{p}_0, \quad y = \zeta_\pm(\theta). \tag{4.5b}$$

Integrate (4.5a) from $y = \zeta_-$ to ζ_+ and use the boundary conditions (4.5b) to get, on the left,

$$\int_{\zeta_-(\theta)}^{\zeta_+(\theta)} (U \sin\theta \, \partial_y \bar{p}_1 - D_{yy} \, \partial_y^2 \bar{p}_1) \, \mathrm{d}y$$

$$= \left[U \sin\theta \, \bar{p}_1 - D_{yy}(\theta) \, \partial_y \bar{p}_1 \right]_{\zeta_-(\theta)}^{\zeta_+(\theta)}$$

$$= -\zeta'_+(\theta) \, \partial_\theta \bar{p}_0(\theta, \zeta_+(\theta)) + \zeta'_-(\theta) \, \partial_\theta \bar{p}_0(\theta, \zeta_-(\theta)). \tag{4.6}$$

On the right, the integral of the term $\partial_\theta^2 \bar{p}_0$ is

$$\int_{\zeta_-(\theta)}^{\zeta_+(\theta)} \partial_\theta^2 \bar{p}_0 \, \mathrm{d}y = \partial_\theta \int_{\zeta_-(\theta)}^{\zeta_+(\theta)} \partial_\theta \bar{p}_0 \, \mathrm{d}y - \zeta'_+(\theta) \, \partial_\theta \bar{p}_0(\theta, \zeta_+(\theta)) + \zeta'_-(\theta) \, \partial_\theta \bar{p}_0(\theta, \zeta_-(\theta)). \tag{4.7}$$

Combining the last two equations, we obtain

$$\partial_T \int_{\zeta_-(\theta)}^{\zeta_+(\theta)} \bar{p}_0 \, \mathrm{d}y = \partial_\theta \int_{\zeta_-(\theta)}^{\zeta_+(\theta)} \partial_\theta \bar{p}_0 \, \mathrm{d}y. \tag{4.8}$$

We can then carry out the y integral on the right of (4.8) after using (4.4), to get

$$\int_{\zeta_-(\theta)}^{\zeta_+(\theta)} \left(\partial_\theta Q + \sigma'(\theta) Q \, y \right) \mathrm{e}^{\sigma(\theta) y} \, \mathrm{d}y = w(\theta) \, \partial_\theta Q - v(\theta) Q, \tag{4.9a}$$

where we defined the weight

$$w(\theta) = \int_{\zeta_-(\theta)}^{\zeta_+(\theta)} \mathrm{e}^{\sigma(\theta) y} \, \mathrm{d}y = \left(\exp(\sigma(\theta) \zeta_+(\theta)) - \exp(\sigma(\theta) \zeta_-(\theta)) \right) / \sigma(\theta), \tag{4.10a}$$

and the drift

$$v(\theta) = -\sigma'(\theta) \int_{\zeta_-(\theta)}^{\zeta_+(\theta)} y \, \mathrm{e}^{\sigma(\theta) y} \, \mathrm{d}y$$

$$= -\frac{\sigma'(\theta)}{\sigma(\theta)} \left(\left[y \, \mathrm{e}^{\sigma(\theta) y} \right]_{\zeta_-(\theta)}^{\zeta_+(\theta)} - \int_{\zeta_-(\theta)}^{\zeta_+(\theta)} \mathrm{e}^{\sigma(\theta) y} \, \mathrm{d}y \right)$$

$$= \frac{\sigma'(\theta)}{\sigma(\theta)} \left(w(\theta) - \exp(\sigma(\theta) \zeta_+(\theta)) \zeta_+(\theta) + \exp(\sigma(\theta) \zeta_-(\theta)) \zeta_-(\theta) \right). \tag{4.10b}$$

Note that $w(\theta) > 0$ if $\zeta_+(\theta) > \zeta_-(\theta)$, and $w(\theta) = 0$ if and only if $\zeta_+(\theta) = \zeta_-(\theta)$. Thus, $w(\theta)$ only vanishes when the domain 'pinches off', as described in § 2.2.2. Despite the

apparent singularity, the weight w is non-singular when σ is small

$$w(\theta) \sim \zeta_+(\theta) - \zeta_-(\theta), \quad \sigma \to 0. \tag{4.11}$$

Another convenient form for the drift ν is

$$\nu(\theta) = w(\theta) \frac{\sigma'(\theta)}{\sigma(\theta)} \left[1 - \frac{\sigma(\theta)}{2 \sinh \Delta(\theta)} \left(e^{\Delta(\theta)} \zeta_+(\theta) - e^{-\Delta(\theta)} \zeta_-(\theta) \right) \right], \tag{4.12}$$

with

$$\Delta(\theta) := \tfrac{1}{2} \sigma(\theta)(\zeta_+(\theta) - \zeta_-(\theta)). \tag{4.13}$$

The function ν appears singular as $\Delta \to 0$, but the limit exists

$$\frac{\nu(\theta)}{w(\theta)} \sim -\tfrac{1}{2} \sigma'(\theta)(\zeta_+(\theta) + \zeta_-(\theta)), \quad \Delta \to 0. \tag{4.14}$$

This expression is valid whether Δ vanishes owing to $\sigma(\theta) = 0$ or $\zeta_+(\theta) = \zeta_-(\theta)$.

Doing the y integral on the left of (4.8), we finally obtain the reduced equation

$$w(\theta) \, \partial_T Q + \partial_\theta (\nu(\theta) Q - w(\theta) \, \partial_\theta Q) = 0. \tag{4.15}$$

The reduced equation is a $(1 + 1)$-dimensional drift-diffusion PDE that captures the time evolution of the marginal probability density

$$P(\theta, T) = \int_{\zeta_-(\theta)}^{\zeta_+(\theta)} \bar{p}_0(\theta, y, T) \, \mathrm{d}y = w(\theta) \, Q(\theta, T). \tag{4.16}$$

The weight function $w(\theta)$ and drift $\nu(\theta)$ encode the effect of the shape of the configuration space.

We can transform (4.15) into an equation for P

$$\partial_T P + \partial_\theta (\mu(\theta) P - \partial_\theta P) = 0, \tag{4.17}$$

with

$$w(\theta) \, \mu(\theta) := \nu(\theta) + w'(\theta) = \exp(\sigma(\theta) \zeta_+(\theta)) \zeta'_+(\theta) - \exp(\sigma(\theta) \zeta_-(\theta)) \zeta'_-(\theta). \tag{4.18}$$

An explicit form for μ in terms of Δ in (4.13) is

$$\mu(\theta) = \frac{\sigma(\theta)}{2 \sinh \Delta(\theta)} \left(e^{\Delta(\theta)} \zeta'_+(\theta) - e^{-\Delta(\theta)} \zeta'_-(\theta) \right). \tag{4.19}$$

Although (4.17) is slightly nicer than (4.15), it has the disadvantage that it requires a derivative $w'(\theta)$ in $\mu(\theta)$, which can cause problems for non-smooth swimmer shapes.

EXAMPLE 4.1 ($\mu(\theta)$ for elliptical and needle swimmers). *For the elliptical swimmer described by* (2.16), *we have*

$$\mu_{ellipse}(\theta) = -\frac{1}{2} e^2 \frac{a\sigma(\theta) \sin 2\theta}{\sqrt{1 - e^2 \cos^2 \theta}} \coth \Delta(\theta) + X_{rot} \, \sigma(\theta) \cos \theta, \tag{4.20}$$

with $\Delta(\theta) = \tfrac{1}{2} \sigma(\theta)(L - 2a\sqrt{1 - e^2 \cos^2 \theta})$. *Note that* μ *vanishes when* $e = 0$ *(circular or point swimmer). The needle is the limit of* (4.20) *as* $e \to 1$

$$\mu_{needle}(\theta) = -a\sigma(\theta) \cos \theta \, sgn\theta \coth \Delta(\theta) + X_{rot} \, \sigma(\theta) \cos \theta. \tag{4.21}$$

These are plotted in figure 6. Note that $\mu_{needle}(\theta)$ *is discontinuous at* $\theta = 0$, *due to the singular derivative of w in* (4.18).
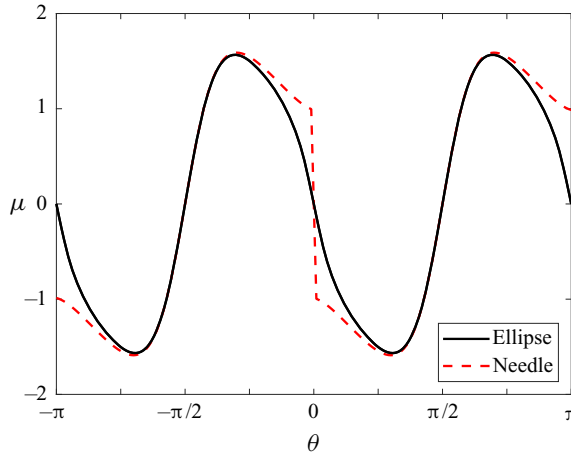
916 A15-16

Figure 6. The angular drift $\mu_{ellipse}(\theta)$ ((4.20)) in a channel of width $L = 1.2$ for an ellipse with $a = 1/2$, $b = 1/8$, $U = D_X = D_Y = 1$, $X_{rot} = -1/4$. The dashed line is $\mu_{needle}(\theta)$ ($b = 0$, (4.21)).

5. Invariant density

A natural quantity to compute from the reduced equation (4.15) is the invariant density for the swimmer. This is the time-independent solution $Q(\theta, T) = \mathcal{Q}(\theta)$ to (4.15)

$$\frac{\mathrm{d}}{\mathrm{d}\theta} \left(v(\theta)\,\mathcal{Q}(\theta) - w(\theta)\,\mathcal{Q}'(\theta) \right) = 0. \tag{5.1}$$

The value of $\mathcal{Q}$ is unique for a periodic domain Ω or a single component Ω_i; see § 2.2. Note that $\mathcal{Q}$ (and hence the invariant density) is independent of D_θ at leading order.

To find the invariant density, we first integrate (5.1) once to get

$$v(\theta)\,\mathcal{Q}(\theta) - w(\theta)\,\mathcal{Q}'(\theta) = c_2. \tag{5.2}$$

The solution to (5.2) then can be written

$$\mathcal{Q}(\theta) = c_1\,(1 - c_2\,F(\theta))\,\mathrm{e}^{\Phi(\theta)}, \tag{5.3}$$

where

$$\Phi(\theta) := \int_{\theta^L}^{\theta} \frac{v(\vartheta)}{w(\vartheta)}\,\mathrm{d}\vartheta, \quad F(\theta) := \int_{\theta^L}^{\theta} \frac{\mathrm{d}\vartheta}{c_1 w(\vartheta)\,\mathrm{e}^{\Phi(\vartheta)}} \tag{5.4}$$

and θ^L is the left-most domain limit ($\theta^L = -\pi$ for Ω and $\theta^L = \theta_i^L$ for Ω_i; see § 2.2). The integrand in (5.4) appears singular as $\Delta \to 0$, but the limit exists as we saw in (4.14).

Next we need to determine the constants c_1 and c_2. Normalization of $\mathcal{P} := w\mathcal{Q}$ determines c_1, but c_2 depends on whether we have an open or closed-channel configuration space (§ 2.2). We treat these two cases separately.

5.1. *Open channel*

For the open-channel configuration space as described in § 2.2.1, $w(\theta)$ and $v(\theta)$ are 2π-periodic. The boundary condition on $\mathcal{Q}(\theta)$ is that it be periodic as well.
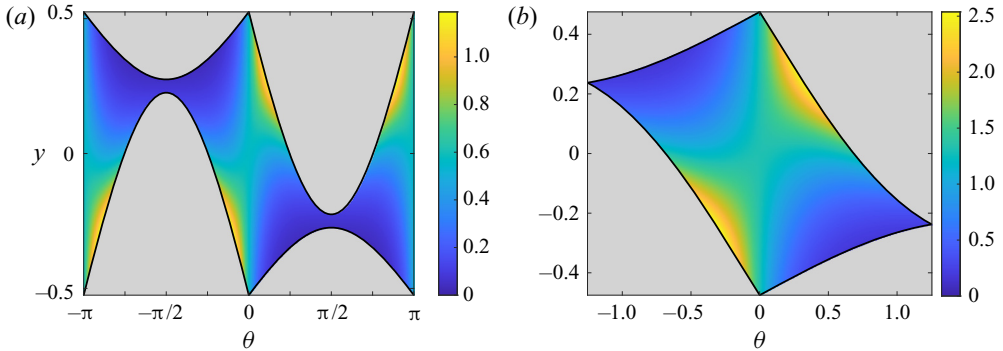
Figure 7. Invariant density $\bar{p}_0 = \mathcal{Q}(\theta)\,e^{\sigma(\theta)y}$ for $U = 1$ and $D_X = D_Y = 0.1$ for the needle in figure 4(*b*) of length $\ell = 2a = 1$ in (*a*) an open channel of width $L = 1.05$; (*b*) a closed channel of width $L = 0.95$, for the domain Ω_1 in figure 5(*b*).

Choosing $\theta^L = -\pi$ in (5.4), we have

$$\mathcal{Q}(-\pi) = c_1 = \mathcal{Q}(\pi) = c_1\,(1 - c_2\,F(\pi))\,e^{\Phi(\pi)}. \tag{5.5}$$

We solve for c_2 in (5.5) to obtain

$$c_2 = \left(1 - e^{-\Phi(\pi)}\right)/F(\pi), \tag{5.6}$$

and

$$\mathcal{Q}(\theta) = c_1\,e^{\Phi(\theta)}\left(1 - \left(1 - e^{-\Phi(\pi)}\right)F(\theta)/F(\pi)\right). \tag{5.7}$$

The constant c_1 is chosen to enforce the normalization of $\mathcal{P} = w\mathcal{Q}$

$$\int_{-\pi}^{\pi}\int_{\zeta_-(\theta)}^{\zeta_+(\theta)} \bar{p}_0(\theta, y)\,\mathrm{d}y\,\mathrm{d}\theta = \int_{-\pi}^{\pi} \mathcal{P}(\theta)\,\mathrm{d}\theta = 1. \tag{5.8}$$

If $\Phi(\theta)$ happens to be 2π-periodic, then we have $\Phi(\pi) = 0$, so $c_2 = 0$ and

$$\mathcal{Q}(\theta) = c_1\,e^{\Phi(\theta)}, \quad (\Phi(\theta)\ 2\pi\text{-periodic}). \tag{5.9}$$

The invariant probability density in this case satisfies detailed balance (Pavliotis 2014). In fact $\Phi(\theta)$ is periodic for the very important case of a left–right symmetric swimmer, for then we have $\zeta_+(\theta) = -\zeta_-(-\theta)$, which follows from symmetries (2.18) and (2.21). This leads to $\Delta(-\theta) = -\Delta(\theta)$ and the integrand of (5.4) is odd in θ. Choosing $\theta^L = -\pi$ then gives $\Phi(-\pi) = \Phi(\pi) = 0$, i.e. Φ is periodic.

From $\mathcal{Q}$, we can reconstruct the full invariant density from (4.4) as $\bar{p}_0(\theta, y) = \mathcal{Q}(\theta)\,e^{\sigma(\theta)y}$, with $\sigma(\theta) = U\sin\theta/D_{yy}(\theta)$. The exponential term reflects the accumulation near both walls, as observed in experiments and simulations. The thickness of the boundary layer is $D_{yy}/U\sin\theta$, which agrees qualitatively with the results for a spherical swimmer in Elgeti & Gompper (2013) and Ezhilan & Saintillan (2015). A typical invariant density in an open-channel configuration is shown in figure 7(*a*) for a needle swimmer. The marginal invariant probability density $\mathcal{P}(\theta)$ is plotted in figure 8(*a*) for elliptical swimmers with different velocities U and centres of rotation X_{rot}. From figure 7, the invariant marginal density in y peaks near both walls, but not exactly at the walls, in accordance with the simulations in the appendix of Ezhilan & Saintillan (2015).
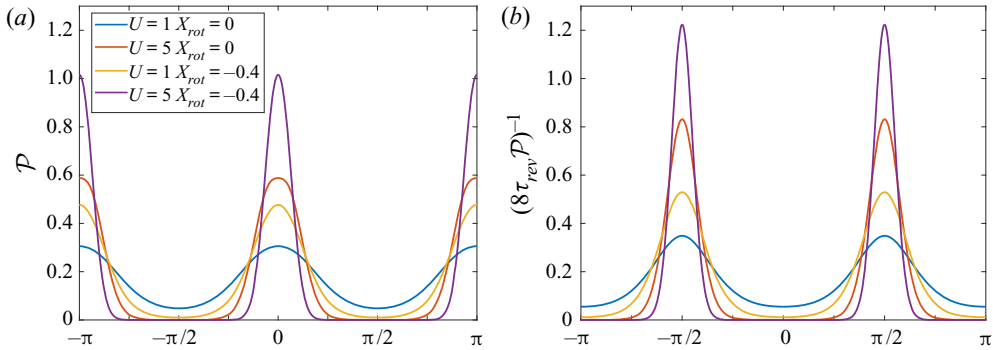
Figure 8. For an ellipse with $a = 2b = 1/2$, $D_X = D_Y = 0.1$, $D_\theta = 0.01$, $U = 1$, in a channel of width $L = 1.2$: (*a*) marginal invariant probability density $\mathcal{P}(\theta)$; (*b*) $1/\mathcal{P}$, normalized to unit area (see (6.8) for definition of τ_{rev}).

What is the meaning of non-zero c_2? It represents an average rotational drift of the needle's stochastic angle $\theta(t)$. To see this, note that in the equilibrium state we have the expectation

$$\mathbb{E}\mu(\theta(T)) = \int_{-\pi}^{\pi} \mu(\theta) \, \mathcal{P}(\theta) \, \mathrm{d}\theta = \int_{-\pi}^{\pi} (\mathcal{P}'(\theta) + c_2) \, \mathrm{d}\theta = 2\pi c_2, \qquad (5.10)$$

since $\mu \mathcal{P} - \mathcal{P}' = c_2$ and $\mathcal{P}(\theta)$ is periodic. Hence, the average rate of angular rotation of the swimmer is $\omega = 2\pi c_2$. From (5.4), the periodic average of $\mu(\theta)$ is

$$\bar{\mu} = \frac{1}{2\pi} \int_{-\pi}^{\pi} \mu(\theta) \, \mathrm{d}\theta = \frac{1}{2\pi} \int_{-\pi}^{\pi} \frac{\nu(\theta)}{w(\theta)} \, \mathrm{d}\theta = \frac{\Phi(\pi)}{2\pi} = \frac{1}{2\pi} \log(1 - c_2 F(\pi))^{-1}, \quad (5.11)$$

which is zero if and only if $c_2 = 0$ ((5.6)).

EXAMPLE 5.1 (invariant density for fast needle swimmer). *It is in general quite challenging to get closed-form solutions for the invariant density of a swimmer, but it can be done in the large-U limit. From (5.4) and (4.18) we have*

$$\Phi(\theta) = \int_{-\pi}^{\theta} \mu(\vartheta) \, \mathrm{d}\vartheta - \log w(\theta) + const., \qquad (5.12)$$

and so the leading-order invariant marginal density $\mathcal{P} = c_1 w \, \mathrm{e}^{\Phi}$ for a left–right-symmetric swimmer is

$$\mathcal{P}(\theta) = \bar{c}_1 \exp\left(\int_{-\pi}^{\theta} \mu(\vartheta) \, \mathrm{d}\vartheta\right), \qquad (5.13)$$

with $\bar{c}_1$ a normalization constant. For large U, the constant $\bar{c}_1$ can be determined by approximating the normalization integral using the maxima of μ.

We illustrate this here for the needle swimmer of examples 2.1 and 4.1. For large U, we can approximate $\coth \Delta \approx sgn(\theta)$ *for $\mu = \mu_{needle}$ in (4.21), and we have*

$$\mu(\theta) \approx -\sigma(\theta) \cos\theta \, (a - X_{rot}), \qquad U \to \infty, \qquad (5.14)$$

with σ defined in (4.4), and $a = \ell/2$ the needle half-length. Note that the channel width L does not appear in (5.14) at leading order in large U: the needle spends most of its time
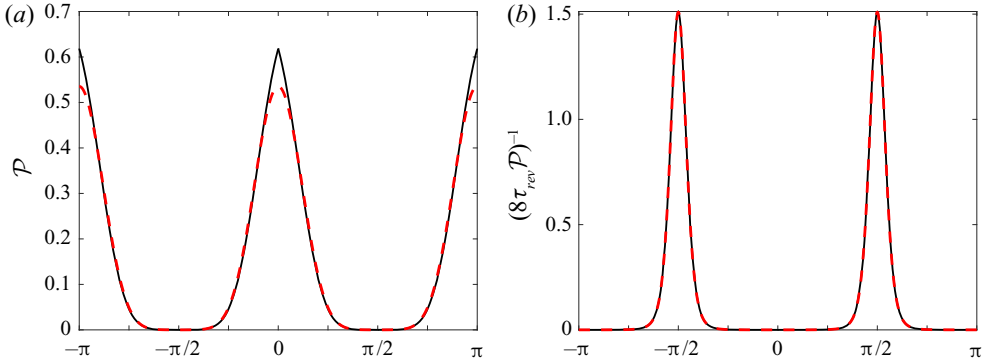
Figure 9. For a needle with $\ell = 1$, $U = 8$, $D_X = 0.1$, $D_Y = 1$, $D_\theta = 0.01$, in a channel of width $L = 1.2$ ($\beta = 3.6$): (*a*) marginal invariant probability density $\mathcal{P}(\theta)$ (solid) and large-U form (5.17) (dashed). Notice the discrepancy near $\theta = 0, \pi$, which goes away for large U. (*b*) Value of $1/\mathcal{P}$, normalized to unit area, for the same parameters.

stuck to one of the walls, so the channel width is not important. We can integrate (5.14) *and use the result in* (5.13) *to find*

$$\mathcal{P}(\theta) = \bar{c}_1 \exp\left(\beta \log\left(\alpha \sin^2\theta + \cos^2\theta\right)^{1/(1-\alpha)}\right), \tag{5.15}$$

with

$$\alpha := D_X/D_Y, \quad \beta := U(a - X_{rot})/2D_Y \gg 1. \tag{5.16}$$

We can see that 'large U' in non-dimensional terms means large β, which is a Péclet number that accounts for the position of the centre of rotation: β is maximized when the centre of rotation is at the rear ($X_{rot} = -a$), which is a rear-rotating swimmer. We can now use Laplace's method to find the normalization constant $\bar{c}_1$. The maxima of the argument of the exponential in (5.15) *correspond to the zeros of μ at $\theta = 0$ and π (with $-a \leq X_{rot} < a$). We thus find*

$$\mathcal{P}(\theta) = \sqrt{\frac{\beta}{4\pi}} \left(\alpha \sin^2\theta + \cos^2\theta\right)^{\beta/(1-\alpha)}, \quad \beta \gg 1. \tag{5.17}$$

In the limit $\alpha = 1$ (equal diffusivities), (5.17) *simplifies to*

$$\mathcal{P}(\theta) = \sqrt{\frac{\beta}{4\pi}} \, \mathrm{e}^{-\beta \sin^2\theta}, \quad \beta \gg 1. \tag{5.18}$$

Note that the limit $\alpha \to 0$ in (5.17) *is well defined and gives $\mathcal{P}(\theta) = \sqrt{\beta/4\pi} \, |\cos\theta|^{2\beta}$. However, the limit $\alpha \to \infty$ gives an improperly normalized density, indicating that the limits $\beta, \alpha \to \infty$ do not commute. (The quartic term in a Taylor series expansion of the log in* (5.15) *has coefficient proportional to α, and cannot be neglected when applying Laplace's method.)*

In figure 9 we compare a numerical solution for $\mathcal{P}$ to the large-U form (5.17)*.*

There is some discrepancy near $\theta = 0, \pi$, which comes from the approximation (5.14) *breaking down near those points, but the difference vanishes as U gets larger. We also plot $1/\mathcal{P}$, which we shall need in §6, for which the approximation is uniformly much better.*

EXAMPLE 5.2 (invariant density for fast circular swimmer). *When the swimmer is perfectly circular, putting $e = 0$ in (4.20) gives $\mu(\theta) = X_{rot}\,\sigma(\theta)\cos\theta$, which is the same as (5.14) with $a = 0$ in the previous example, except that here this expression is exact. The invariant density thus has the form (5.15), with $\beta = -UX_{rot}/2D_Y$, which can have either sign. For $\beta \gg 1$ we recover (5.17) and (5.18) – the circular swimmer tends to align parallel to the wall. For $-\beta \gg 1$ the maxima of $\int \mu\,\mathrm{d}\theta$ switch from $\{0, \pi\}$ to $\pm\pi/2$, and we get instead of (5.17)*

$$\mathcal{P}(\theta) = \sqrt{\frac{|\beta|}{4\pi\alpha}}\left(\sin^2\theta + \alpha^{-1}\cos^2\theta\right)^{-|\beta|/(1-\alpha)}, \quad -\beta \gg 1, \tag{5.19}$$

which for $\alpha = 1$ simplifies to

$$\mathcal{P}(\theta) = \sqrt{\frac{|\beta|}{4\pi}}\,\exp(-|\beta|\cos^2\theta), \quad -\beta \gg 1. \tag{5.20}$$

Comparing the latter to (5.18), we can see that fast front-rotating circular swimmers ($X_{rot} > 0$) collect at $\theta = \pm\pi/2$, swimming towards the wall, rather than aligning parallel to the wall. The limit $\alpha \to 0$ in 5.19 gives $\mathcal{P}(\theta) = \frac{1}{2}\left(\delta(\theta - \pi/2) + \delta(\theta + \pi/2)\right)$.

5.2. Closed channel

For a closed-channel configuration space, as described in §2.2.2, the domain is given by Ω_i in (2.25), for some fixed i. Now the boundary condition is that there be no net flux in the θ direction, so the constant $c_2 = 0$ in (5.2). The solution for the invariant density is thus

$$\mathcal{Q}(\theta) = c_1\,\mathrm{e}^{\Phi(\theta)}, \quad \theta_i^L \le \theta \le \theta_i^R, \tag{5.21}$$

with c_1 obtained by the normalization condition for $\mathcal{P} = w\mathcal{Q}$

$$\int_{\theta_i^L}^{\theta_i^R} \int_{\zeta_-(\theta)}^{\zeta_+(\theta)} \bar{p}_0(\theta, y)\,\mathrm{d}y\,\mathrm{d}\theta = \int_{\theta_i^L}^{\theta_i^R} \mathcal{P}(\theta)\,\mathrm{d}\theta = 1. \tag{5.22}$$

A typical invariant density in a closed-channel configuration is shown in figure 7(b) for a needle swimmer.

6. Mean exit times and MRTs

A standard problem in drift-diffusion processes is to compute the mean exit time (MET) of a particle to some exit, also called a first-passage time (Ward & Keller 1993; Redner 2001; Holcman & Schuss 2014; Kurella *et al.* 2015; Grebenkov 2016; Marcotte *et al.* 2018). Associated with the reduced drift-diffusion equation (4.17) is a reduced equation for the mean exit time $\tau(\theta)$

$$\mu(\theta)\tau' + \tau'' = -1, \quad \theta^L < \theta < \theta^R, \tag{6.1a}$$

$$\tau(\theta^L) = \tau(\theta^R) = 0. \tag{6.1b}$$

The left-hand side of (6.1a) is the adjoint of the linear operator in (4.17) (Redner 2001; Holcman & Schuss 2014; Kurella *et al.* 2015). The solution to (6.1) gives the expected time τ for a particle starting at θ (for any y) to reach an 'exit' at $\theta = \theta^L$ or $\theta = \theta^R$. Note that since $T = D_\theta t$ in (4.17) the dimensional MET is τ/D_θ, which goes to infinity as $D_\theta \to 0$, i.e. the exit cannot be reached if $D_\theta = 0$. The word exit here is interpreted loosely: the MET merely signifies the first time a swimmer's orientation achieves the value θ^L or θ^R, starting from some value θ.

6.1. *Solving the MET equation*

To solve (6.1), define $T = w\tau'$ which satisfies

$$(\nu/w)\, T + T' = -w, \quad T = w\tau', \tag{6.2}$$

where $w(\theta)$ and $\nu(\theta)$ are defined in (4.10). Use the integrating factor $\tilde{c}_1\, e^{\Phi(\theta)}$ from (5.4) to get

$$\tau'(\theta) = -\frac{1}{\tilde{\mathcal{P}}(\theta)}\left(\tilde{G}(\theta) - \mathcal{C}\right), \quad \tilde{G}(\theta) := \int_{\theta^L}^{\theta} \tilde{\mathcal{P}}(\vartheta)\, d\vartheta, \tag{6.3}$$

where $\tilde{\mathcal{P}}(\theta) = \tilde{c}_1\, w\, e^{\Phi}$ is analogous to the invariant density for a closed channel (5.21) and $\mathcal{C}$ is an integration constant. We choose $\tilde{c}_1$ so that the normalization condition (5.22) is satisfied: $\tilde{G}(\theta^R) = 1$; hence, $\tilde{G}(\theta)$ is the equilibrium probability of finding the swimmer between θ^L and θ, if the channel were closed. The MET τ has a unique maximum at $\theta = \theta_*$ with $\mathcal{C} = \tilde{G}(\theta_*)$.

Now integrate (6.3)

$$\tau(\theta) = \int_{\theta^L}^{\theta} \frac{1}{\tilde{\mathcal{P}}(\vartheta)}\left(\mathcal{C} - \tilde{G}(\vartheta)\right)\, d\vartheta, \tag{6.4}$$

which satisfies the left boundary condition $\tau(\theta^L) = 0$. The right boundary condition then requires $\tau(\theta^R) = 0$, which fixes the integration constant

$$\mathcal{C} = \int_{\theta^L}^{\theta^R} \frac{\tilde{G}(\vartheta)}{\tilde{\mathcal{P}}(\vartheta)}\, d\vartheta \left/ \int_{\theta^L}^{\theta^R} \frac{d\vartheta}{\tilde{\mathcal{P}}(\vartheta)}\right. . \tag{6.5}$$

Equations (6.4) and (6.5) give the MET for a swimmer starting at θ and exiting at either θ^L or θ^R. We now focus on a particular version of this mean exit time with a more natural interpretation – the MRT.

6.2. *Mean reversal time*

The MRT τ_{rev} (or turnaround time (Holcman & Schuss 2014)) is the expected time for a swimmer initially oriented with $\theta = 0$ to reverse direction to $\theta = \pm\pi$. It can be obtained from (6.4) by setting $-\theta^L = \theta^R = \pi$ and $\theta = 0$

$$\tau_{rev} = \tau(0) = \int_{-\pi}^{0} \frac{1}{\tilde{\mathcal{P}}(\vartheta)}\left(\mathcal{C} - \tilde{G}(\vartheta)\right)\, d\vartheta. \tag{6.6}$$

In Appendix A we show how the constant $\mathcal{C}$ can be eliminated to obtain

$$\tau_{rev} = \frac{\tilde{G}(0)}{1 + e^{\pi\bar{\mu}}} \int_{-\pi}^{0} \frac{d\vartheta}{\tilde{\mathcal{P}}(\vartheta)} + \tanh(\pi\bar{\mu}/2) \int_{-\pi}^{0} \frac{\tilde{G}(\vartheta)}{\tilde{\mathcal{P}}(\vartheta)}\, d\vartheta, \tag{6.7}$$

where $\bar{\mu}$ is defined in (5.11). For a left–right-symmetric swimmer, $\tilde{\mathcal{P}} = \mathcal{P}$, $\bar{\mu} = 0$ and $\tilde{G}(0) = 1/2$ by symmetry, so we obtain the compact expression

$$\tau_{rev} = \frac{1}{4} \int_{0}^{\pi} \frac{d\theta}{\mathcal{P}(\theta)}. \tag{6.8}$$
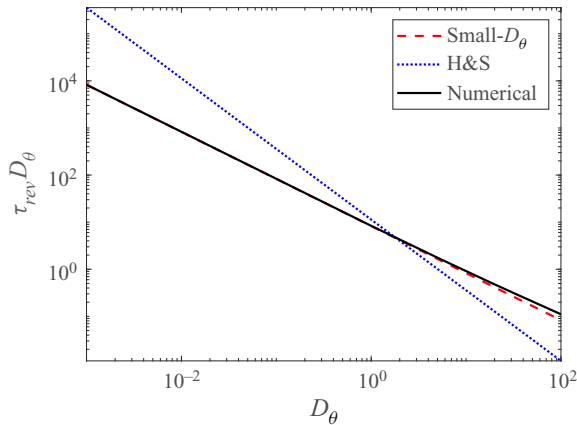
Figure 10. MRT for a needle as a function of D_θ, for $\lambda = 0.9$, $D_Y = 1$. The dashed line is (6.11), which is technically valid for small D_θ but applies over a wide range. The dotted line is from Holcman & Schuss (2014). The solid line is from a finite-element simulation of the full PDE.

EXAMPLE 6.1 (MRT with diffusion only). *In the absence of swimming ($U = 0$), we have $v = 0$ from (4.10b), and $\tilde{\mathcal{P}} = \mathcal{P} = c_1 w$, with $c_1^{-1} = \int_{-\pi}^{\pi} w \, d\theta$. Hence, (6.8) is*

$$\tau_{rev} = \frac{1}{2} \left(\int_0^\pi w(\theta) \, d\theta \right) \left(\int_0^\pi \frac{d\theta}{w(\theta)} \right). \tag{6.9}$$

For a needle with wall distance function (2.8), we get from (2.20)

$$w(\theta) = \zeta_+(\theta) - \zeta_-(\theta) = L - \ell \, |\sin \theta| \tag{6.10}$$

where X_{rot} drops out: the centre of rotation is immaterial in the absence of swimming. We can then easily compute the integral (6.9) to obtain

$$\tau_{rev} = \frac{(\pi - 2\lambda)(\pi - \arccos \lambda)}{\sqrt{1 - \lambda^2}}, \quad \lambda := \ell/L < 1. \tag{6.11}$$

The 'narrow exit' limit corresponds to $\lambda = 1 - \delta$, with δ small

$$\tau_{rev} = \frac{\pi(\pi - 2)}{\sqrt{2\delta}} + O(\delta^0), \quad \delta \ll 1. \tag{6.12}$$

This is similar but not identical to Holcman & Schuss's result (Holcman & Schuss 2014, (5.13))

$$\tau_{rev} = \frac{\pi(\pi - 2)}{\sqrt{2\delta}} \sqrt{\frac{D_Y}{2L^2 D_\theta}}, \tag{6.13}$$

valid as $\delta \to 0$, but otherwise unconstrained. In figure 10, a comparison to a finite-element numerical solution of the full PDE (i.e. without using the reduced equation) shows excellent agreement with our small-D_θ form (6.11), but less so with the form (6.13). Possibly there is a parameter regime where (6.13) shows better agreement.
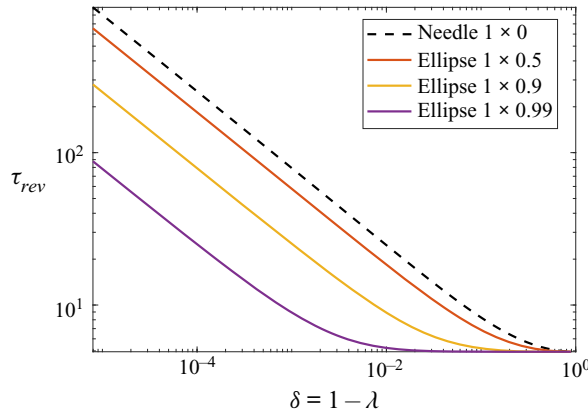
916 A15-23

Figure 11. MRT τ_{rev} for a needle and different ellipses, as a function of gap size δ. An ellipse reverses more rapidly as it becomes more circular, since it spends less time aligning with the wall.

For an elliptical shape (2.16) *with* $U = 0$, *we have*

$$w(\theta) = L\left(1 - \lambda\sqrt{1 - e^2\cos^2\theta}\right). \tag{6.14}$$

Then

$$L^{-1}\int_0^\pi w(\theta)\,d\theta = \pi - 2\lambda E(e), \tag{6.15}$$

where E is a complete elliptic integral of the second kind. We also have

$$\int_0^\pi \frac{L\,d\theta}{w(\theta)} = \frac{\pi}{\sqrt{(1-\lambda^2)(1-(1-e^2)\lambda^2)}} - \frac{2}{\lambda}K(e) + \frac{2}{\lambda(1-\lambda^2)}\,\Pi\left(\frac{e^2}{1-\lambda^{-2}}\,\bigg|\,e\right), \tag{6.16}$$

where K and Π are the complete elliptic integrals of the first and third kinds. Together, the product of (6.15) *and* (6.16) *into* (6.9) *gives the reversal time for an ellipse. The MRT for a needle is compared to different ellipses in figure 11.*

6.3. Asymptotics of MRT

The integrand in (6.8) is the inverse of $\mathcal{P}(\theta) = c_1 w(\theta)\,e^{\Phi(\theta)}$. The integral itself will thus typically be dominated by the minima of $\mathcal{P}$, which correspond to values of θ that the swimmer finds difficult to cross when trying to reverse. This could be because $\delta = 1 - \ell/L$ is small: this is the narrow escape problem discussed by Holcman & Schuss (2014) (see example 6.1). However, for a swimmer the long reversal time is usually due to a swimmer 'sticking' to the top or bottom wall for long times.

To approximate the integral in (6.8), we look for minima θ_* of $\mathcal{P}(\theta)$, where we can approximate

$$\mathcal{P}(\theta) = \mathcal{P}(\theta_*)\exp(C_*\xi^2 + O(\xi^3)), \quad \xi = \theta - \theta_*. \tag{6.17}$$

This gives us the approximation

$$\tau_{rev} \approx \frac{1}{4\mathcal{P}(\theta_*)}\int_{-\infty}^\infty e^{-C_*\xi^2}\,d\vartheta = \frac{1}{4\mathcal{P}(\theta_*)}\sqrt{\frac{\pi}{C_*}}. \tag{6.18}$$

916 A15-24

This should be multiplied by the number of minima with value $\mathcal{P}(\theta_*)$ in $0 \leq \theta < \pi$, should there be more than one. We can easily obtain a more accurate, if messier, approximation by retaining higher-order terms in (6.17).

EXAMPLE 6.2 (MRT for a fast needle swimmer). *An ideal example for the asymptotic approximation of τ_{rev} is the fast needle swimmer of example 5.1. Figure 9(b) clearly shows strong peaks in $1/\mathcal{P}$ at $\theta_* = \pm\pi/2$ even for this modest value of U. Hence, we are justified in expanding around the minimum of (5.17) at $\theta_* = \pi/2$, which gives*

$$\mathcal{P}(\theta_*) = \sqrt{\frac{\beta}{4\pi}}\,\alpha^{\beta/(1-\alpha)}, \quad C_* = \beta/\alpha. \tag{6.19}$$

Recall that $\alpha = D_X/D_Y$ is the ratio of diffusivities, and β is a large Péclet number defined in (5.16). Inserting these in (6.18), we find

$$\tau_{rev} \approx \frac{\pi}{2\beta}\,\alpha^{\frac{1}{2} - \frac{\beta}{1-\alpha}}, \tag{6.20}$$

or in the case $\alpha = 1$

$$\tau_{rev} \approx \frac{\pi}{2\beta}\,\mathrm{e}^{\beta}, \quad \alpha = 1. \tag{6.21}$$

This is exponential in the Péclet number β, so that the reversal time can become extremely long. Note also that the MRT is independent of the channel width L in this limit. For the parameters in figure 9 ($\beta = 3.6$), the numerical MRT is $\tau_{rev} \approx 1.54 \times 10^3$, whereas the approximation (6.20) gives 1.38×10^3. The approximation is thus reasonably good even for a modest Péclet number β.

7. Effective diffusion along the channel

For the open-channel configuration, as a microswimmer travels down the channel, it will occasionally reverse direction. For long times, we expect these reversals to lead to an effective diffusion process on large scales. One way to capture this limit exactly is to derive an effective diffusion equation using a homogenization approach (Sagues & Horsthemke 1986; McCarty & Horsthemke 1988; Childress & Soward 1989; Majda & Kramer 1999). We proceed to do so for our microswimmer in a channel, and find the effective diffusivity in the same reduced limit as in § 4 (small D_θ).

7.1. Homogenized equation

Rewrite the Fokker–Planck (3.3) as

$$\partial_t p + \partial_x(u\,p) + \partial_y(v\,p) = \partial_x^2(D_{xx}\,p) + 2\partial_x\partial_y(D_{xy}\,p) + \partial_y^2(D_{yy}\,p) + \partial_\theta^2(D_\theta\,p), \tag{7.1}$$

where $U = (u, v)$. In this section we only assume that $\boldsymbol{D}$, D_θ and $\boldsymbol{U}$ do not depend on x. (The derivation could easily be extended to allow x dependence.) Later (§ 7.2) we will specialize to the forms in (3.4), which are functions of θ only.

We will homogenize in the x direction only, since the swimmer is confined between walls in the y direction and the θ direction is periodic. We introduce a large scale x/η

and long time t/η^2, where η is a small expansion parameter. After rescaling $t \to t/\eta^2$ and $x \to x/\eta$, (7.1) becomes

$$\mathcal{L} p = -\eta\,\partial_x(u\,p) + 2\eta\,\partial_x\partial_y(D_{xy}\,p) - \eta^2\partial_t p + \eta^2\,\partial_x^2(D_{xx}\,p), \qquad (7.2a)$$

where we defined the linear operator

$$\mathcal{L} p := \partial_y(v\,p) - \partial_y^2(D_{yy}\,p) - \partial_\theta^2(D_\theta\,p). \qquad (7.2b)$$

The no-flux boundary conditions for (7.2a) are

$$\bigl(v\,p - \partial_y(D_{yy}\,p) - \eta\,\partial_x(D_{xy}\,p)\bigr) + \zeta_\pm'(\theta)\,\partial_\theta(D_\theta\,p) = 0, \quad y = \zeta_\pm(\theta). \qquad (7.2c)$$

We expand the probability density p as a regular series in η

$$p = p_0 + \eta\,p_1 + \eta^2\,p_2 + \dots . \qquad (7.3)$$

Define the cell integral of $f(\theta, y)$ as

$$\langle f \rangle := \int_{-\pi}^{\pi}\int_{\zeta_-(\theta)}^{\zeta_+(\theta)} f(\theta, y)\,\mathrm{d}y\,\mathrm{d}\theta. \qquad (7.4)$$

To ensure uniqueness at each order, we enforce the cell-integrated probability $\langle p \rangle = \langle p_0 \rangle$, so that $\langle p_i \rangle = 0$ for $i > 0$.

Now we collect powers of η in (7.2) with the expansion (7.3). At leading order in η we have from (7.2a)

$$\mathcal{L} p_0 = 0, \qquad (7.5a)$$

with boundary conditions from (7.2c)

$$v\,p_0 - \partial_y(D_{yy}\,p_0) + \zeta_\pm'(\theta)\,\partial_\theta(D_\theta\,p_0) = 0, \quad y = \zeta_\pm(\theta). \qquad (7.5b)$$

The operator $\mathcal{L}$ only involves (θ, y), so we can solve (7.5) with

$$p_0 = P(x, t)\,\rho(\theta, y), \quad \mathcal{L}\rho = 0, \quad \langle \rho \rangle = 1, \qquad (7.6)$$

where $\rho(\theta, y)$ is the cell-normalized x-independent invariant density for (7.1), and so $\langle p_0 \rangle = P(x, t)$.

At order η^1, (7.2a) gives

$$\mathcal{L} p_1 = -\partial_x(u\,p_0) + 2\partial_x\partial_y(D_{xy}\,p_0) = \bigl(-u\,\rho + 2\partial_y(D_{xy}\,\rho)\bigr)\,\partial_x P. \qquad (7.7)$$

We can solve this by letting

$$p_1 = \chi\,\partial_x P, \qquad (7.8)$$

where $\chi(\theta, y)$ satisfies the cell problem

$$\mathcal{L}\chi = -u\,\rho + 2\partial_y(D_{xy}\,\rho), \qquad (7.9a)$$

$$0 = v\,\chi - \partial_y(D_{yy}\,\chi) + \zeta_\pm'(\theta)\,\partial_\theta(D_\theta\,\chi) - D_{xy}\,\rho, \quad y = \zeta_\pm(\theta), \qquad (7.9b)$$

with $\langle \chi \rangle = 0$. The solvability condition for the cell problem (7.9) demands

$$\langle u\,\rho \rangle = \bigl\langle \partial_y(D_{xy}\,\rho) \bigr\rangle. \qquad (7.10)$$

In our case, the left and right sides of (7.10) vanish separately after using the channel symmetry $\rho(\theta + \pi, y) = \rho(\theta, -y)$. On the left, we have $u(\theta) = U\cos\theta$, so $u(\theta + \pi) =$

$-u(\theta)$ and the integral must vanish. On the right, we have $D_{xy}(\theta) = \frac{1}{2}(D_X - D_Y)\sin 2\theta$ from (3.4), so $D_{xy}(\theta + \pi) = D_{xy}(\theta)$ and $\partial_y \rho(\theta + \pi, y) = -(\partial_y \rho)(\theta, -y)$ and the integral again vanishes. There is thus no 'ratchet effect' to cause a net drift, since there is no breaking of the left–right symmetry of the channel. Having patterned walls as in Yariv & Schnitzer (2014) and Malgaretti & Stark (2017) would likely cause such a drift.

At order η^2, (7.2) gives

$$\mathcal{L} p_2 = -\partial_x(u p_1) + 2\partial_x\partial_y(D_{xy} p_1) - \partial_t p_0 + \partial_x^2(D_{xx} p_0), \tag{7.11a}$$

$$0 = \left(v p_2 - \partial_y(D_{yy} p_2) - \partial_x(D_{xy} p_1)\right) + \zeta'_\pm(\theta)\, \partial_\theta(D_\theta p_2), \quad y = \zeta_\pm(\theta). \tag{7.11b}$$

The solvability condition then yields the effective heat equation

$$\partial_t P = D_{eff}\, \partial_x^2 P, \tag{7.12}$$

where the effective diffusivity in x is

$$D_{eff} = \langle D_{xx}\,\rho \rangle - \langle u\,\chi \rangle + \left\langle \partial_y(D_{xy}\chi) \right\rangle. \tag{7.13}$$

The solvability condition (7.10) implies that χ only affects the effective diffusivity up to an additive multiple of ρ.

7.2. *Reduced equation limit*

We solve the cell problem (7.9) in the same small-D_θ limit as in § 4. Anticipating that the effective diffusivity should diverge as $\varepsilon = D_\theta$ becomes smaller, we expand

$$\chi = \varepsilon^{-1}\,\chi_0 + \chi_1 + \varepsilon\,\chi_2 + \dots. \tag{7.14}$$

The leading-order ε^{-1} cell problem (7.9) is the same as (4.3), with solution

$$\chi_0(\theta, y) = X(\theta)\, e^{\sigma(\theta)y}. \tag{7.15}$$

At next order ε^0 we have the PDE and boundary conditions

$$U\sin\theta\,\partial_y\chi_1 - D_{yy}(\theta)\,\partial_y^2\chi_1 = \partial_\theta^2\chi_0 - \left(U\cos\theta - 2\sigma D_{xy}\right)\mathcal{Q}(\theta)\,e^{\sigma(\theta)y}; \tag{7.16a}$$

$$U\sin\theta\,\chi_1 - D_{yy}(\theta)\,\partial_y\chi_1 = -\zeta'_\pm(\theta)\,\partial_\theta\chi_0 + D_{xy}\,\mathcal{Q}(\theta)\,e^{\sigma(\theta)y}, \quad y = \zeta_\pm(\theta), \tag{7.16b}$$

where we used the invariant density $\bar{p}_0 = \mathcal{Q}(\theta)\,e^{\sigma(\theta)y}$. Integrate (7.16a) from $y = \zeta_-$ to ζ_+ and use the boundary conditions (7.16b)

$$\partial_\theta(vX - w\,\partial_\theta X) = -\mathcal{E}\,\mathcal{P}, \tag{7.17}$$

where $\mathcal{P} = w\mathcal{Q}$, and

$$\mathcal{E}(\theta) := U\cos\theta - \sigma D_{xy} = \frac{U\cos\theta}{\cos^2\theta + \alpha\sin^2\theta}, \tag{7.18}$$

with $\alpha = D_X/D_Y$ as in (5.17). We integrate (7.17) once

$$vX - w\,\partial_\theta X = d - H(\theta), \quad H(\theta) := \int_{-\pi}^{\theta} \mathcal{E}(\vartheta)\,\mathcal{P}(\vartheta)\,d\vartheta, \tag{7.19}$$

with d a constant of integration. The solvability condition (7.10) ensures that $H(\theta)$ is a periodic function of θ. Next use the integrating factor $e^{\Phi(\theta)}$ from (5.4), with $\theta^L = -\pi$

$$w\,e^\Phi\,\partial_\theta(e^{-\Phi}X) = H(\theta) - d. \tag{7.20}$$

We integrate again and find

$$
e^{-\Phi(\theta)} X(\theta) - X(-\pi) = \int_{-\pi}^{\theta} \frac{H(\vartheta)}{w(\vartheta)\, e^{\Phi(\vartheta)}} \, d\vartheta - c_1 d\, F(\theta), \tag{7.21}
$$

where we used $F(\theta)$ from (5.4). By rearranging and using (5.7), we find after introducing new constants

$$
X(\theta) = \tilde{c}_1\, e^{\Phi(\theta)} \left(\int_{-\pi}^{\theta} \frac{H(\vartheta)}{\tilde{\mathcal{P}}(\vartheta)} \, d\vartheta - d_2 F(\theta) \right) + d_1 \mathcal{Q}(\theta), \tag{7.22}
$$

where we used $\tilde{\mathcal{P}} = \tilde{c}_1 w\, e^{\Phi}$ as in §6.1. The constant d_1 is adjusted to satisfy $\langle \chi \rangle = 0$ and is immaterial to the effective diffusivity. The constant d_2 is used to enforce periodicity of X and can be eliminated to obtain

$$
X(\theta) = \tilde{c}_1\, e^{\Phi(\theta)} \left(\int_{-\pi}^{\theta} \frac{H(\vartheta)}{\tilde{\mathcal{P}}(\vartheta)} \, d\vartheta - \frac{F(\theta)}{F(\pi)} \int_{-\pi}^{\pi} \frac{H(\vartheta)}{\tilde{\mathcal{P}}(\vartheta)} \, d\vartheta \right) + d_1 \mathcal{Q}(\theta). \tag{7.23}
$$

In this reduced limit, the effective diffusivity (7.13) is

$$
D_{eff} = \mathbb{E} D_{xx} + D_{enh}, \quad D_{enh} := -\int_{-\pi}^{\pi} \varXi\, w X \, d\theta, \tag{7.24}
$$

to leading order in D_θ. The expected value $\mathbb{E} D_{xx}$ is taken over the invariant marginal density $\mathcal{P}(\theta)$, and D_{enh} is the 'enhanced' part of the diffusivity.

7.3. *Bounding D_{eff} by τ_{rev} for a left–right-symmetric swimmer*

Since the expressions are getting a bit complicated, for the sake of brevity we will focus on the left–right-symmetric case for this section. In that case the term involving $F(\theta)$ vanishes in (7.23), and $\tilde{c}_1\, e^{\Phi}$ becomes $\mathcal{Q}$

$$
X(\theta) = \mathcal{Q}(\theta) \int_{-\pi}^{\theta} \frac{H(\vartheta)}{\mathcal{P}(\vartheta)} \, d\vartheta + d_1 \mathcal{Q}(\theta). \tag{7.25}
$$

After restoring in (7.25) the definition of H from (7.19), it can be shown that the enhanced diffusivity D_{enh} in (7.24) can be written as

$$
D_{enh} = 4 \int_{0}^{\pi/2} \varXi(\theta)\, \mathcal{P}(\theta) \int_{0}^{\theta} \varXi(\theta')\, \mathcal{P}(\theta') \int_{\theta}^{\pi-\theta} \frac{d\theta''}{\mathcal{P}(\theta'')} \, d\theta'\, d\theta. \tag{7.26}
$$

To derive this we used the symmetries $\varXi(\theta + \pi) = \varXi(\pi - \theta) = -\varXi(\theta)$, $\mathcal{P}(\theta + \pi) = \mathcal{P}(\pi - \theta) = \mathcal{P}(\theta)$, the latter holding for a left–right-symmetric swimmer. Rearranging the inner-most integral in (7.27) gives us

$$
D_{enh} = \frac{1}{2} \tau_{rev} (\mathbb{E}|\varXi|)^2 - 8 \int_{0}^{\pi/2} \varXi(\theta)\, \mathcal{P}(\theta) \int_{0}^{\theta} \varXi(\theta')\, \mathcal{P}(\theta)' \int_{0}^{\theta} \frac{d\theta''}{\mathcal{P}(\theta'')} \, d\theta'\, d\theta, \tag{7.27}
$$

where the MRT τ_{rev} was defined in (6.8). The expected value in (7.27) is taken over the invariant marginal density $\mathcal{P}(\theta)$, as in (7.24).
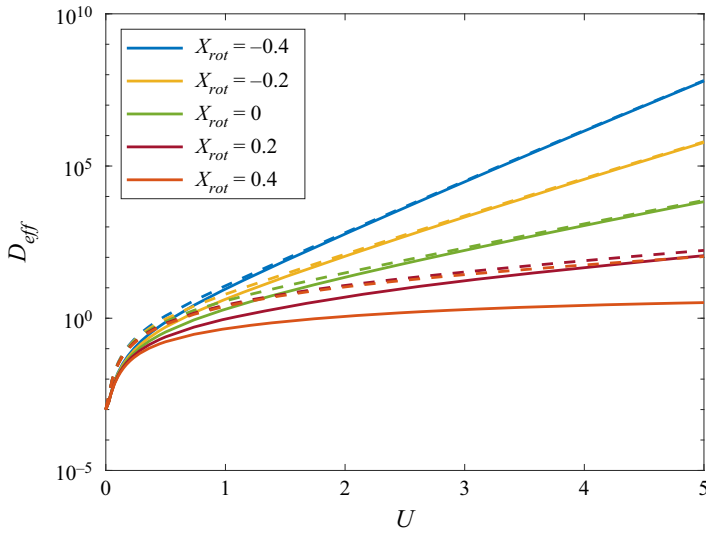
916 A15-28

Figure 12. Effective diffusivity from (7.24) for an ellipse with $a = 1$, $b = 1/2$, $D_X = D_Y = 0.1$, $D_\theta = 0.01$, in a channel of width $L = 1.2$. The dashed lines are the bound $\frac{1}{2}U^2\tau_{rev}$ from (7.28), with $\alpha = 1$ and τ_{rev} given by (6.8). The decrease in exponential rate as the centre of rotation X_{rot} is moved forward is similar to the asymptotic form of τ_{rev} for a needle, (6.21), with β given by (5.16).

Since $\Xi(\theta)$ defined by (7.18) is non-negative in $[0, \pi/2]$, (7.27) immediately gives us the bound

$$D_{enh} \leq \tfrac{1}{2}\tau_{rev}(\mathbb{E}|\Xi|)^2 \leq \tfrac{1}{2}\tau_{rev} \max_\theta \Xi^2(\theta), \tag{7.28a}$$

with

$$\max_{0 \leq \theta \leq \pi/2} \Xi(\theta) = \begin{cases} U, & \alpha \geq 1/2; \\ U/\sqrt{4\alpha(1-\alpha)}, & \alpha < 1/2. \end{cases} \tag{7.28b}$$

This useful bound allows us to estimate D_{enh} from τ_{rev}, which is simpler to compute ((6.8)). The estimate tends to improve the longer the swimmer spends aligned with the walls (figure 12).

8. Hydrodynamic interactions

In this section, we model a swimmer as a point singularity (stresslet) and add hydrodynamic interactions with walls to the ABP model (3.2). Our goal is to examine the importance of including shape in addition to hydrodynamic interactions in a narrow channel. Hydrodynamic interactions modify the velocity and vorticity experienced by the swimmer. The swimmer's shape modifies the configuration space, that is, the allowable range of θ and y values.

Since it is challenging to directly compare invariant densities $\bar{p}(\theta, y)$ for two different shapes, which have different configuration spaces, we compare instead cross-sectional (marginal) invariant densities $\int_{-\pi}^{\pi} \bar{p}(\theta, y) \, d\theta$ for a narrow open channel.

We take the model from Spagnolie *et al.* (2015) where the velocity field of an ellipsoidal swimmer with $X_{rot} = 0$ is approximated by a stresslet with non-dimensional magnitude α. Here $\alpha > 0$ and $\alpha < 0$ represent a pusher and puller, respectively. Using the result in Spagnolie *et al.* (2015) and axial symmetry of the ellipsoid, we can obtain the swimmer's

translational and rotational velocity in a channel. We assume the motion is confined to the x–y plane, even though the hydrodynamic interactions are based on an ellipsoid. Assuming an isotropic spatial diffusion ($D_X = D_Y$), we arrive at the Itô stochastic equation

$$dy = U \sin \theta \, dt - \frac{3U\alpha}{8} \left(\frac{a^2}{(L/2 + y)^2} - \frac{a^2}{(L/2 - y)^2} \right) (1 - 3 \sin^2 \theta) \, dt + \sqrt{2D_X} \, dW_1,$$

$$(8.1a)$$

$$d\theta = -\frac{3U\alpha}{64a} \left(\frac{a^3}{(L/2 + y)^3} + \frac{a^3}{(L/2 - y)^3} \right) [4 - \Gamma (3 - \cos 2\theta)] \sin 2\theta \, dt + \sqrt{2D_\theta} \, dW_2,$$

$$(8.1b)$$

which is a generalization to (3.2) that includes hydrodynamic interactions. Here, $\Gamma = (a^2 - b^2)/(a^2 + b^2) \in [0, 1]$, where a and b are the semi-major and semi-minor axes of the ellipsoid. Equation (8.1) is a far-field approximation, but Spagnolie *et al.* (2015) have shown that this model is surprisingly accurate when a swimmer is near a wall, so we expect (8.1) to be an adequate model for narrow channel confinement. Since the noise is purely additive, we can easily integrate (8.1) using the explicit Euler method for stochastic differential equations (SDEs). We use an adaptive step size that is decreased as the swimmer approaches boundaries. If a step would take the swimmer inside a boundary, that step is rejected, the step size is decreased and new Gaussian random numbers are generated. This 'rejection sampling' approach realizes the no-flux boundary condition at the walls. We integrate over many realizations and for long enough times that the probability density of swimmers closely approximates the invariant density.

Spagnolie *et al.* (2015) argue that, without noise, a puller ($\alpha < 0$) is repelled by a wall when initially aligned parallel to it; it is stable when aligned perpendicular to the wall. The opposite is true for a pusher ($\alpha > 0$). Figure 13 shows cross-sectional invariant densities for various stresslet magnitudes α. In figure 13(*a*) (puller), there is a plateau between $[-0.1, 0.1]$ with small peaks, corresponding to the swimmer accumulating predominantly perpendicular to the wall. The plateau and peaks become more pronounced with a larger stresslet amplitude. Figure 13(*b*) (pusher) shows concentration peaks near both walls, corresponding to parallel alignment, which get closer to the walls as α is increased. Simulations with a wider channel (not shown) agree with past experiments (Berke *et al.* 2008; Li & Tang 2009; Li *et al.* 2011; Gachelin *et al.* 2013) and simulations (Hernandez-Ortiz *et al.* 2005; Nash *et al.* 2010; Costanzo *et al.* 2012; Chilukuri *et al.* 2014; Alonso-Matilla *et al.* 2016).

A simple way to quantify the importance of correctly accounting for the shape of the swimmer is to perform simulations using the configuration space for a spherical swimmer of radius 0.5, but retain hydrodynamic interactions for an ellipsoidal swimmer. This artificial situation is not meant to model a real swimmer, but is merely used to confirm that the shape of configuration space plays an important role in the final results. Figure 14 shows the cross-sectional invariant densities for that case, and we can see that a pusher (figure 14*b*) no longer exhibits parallel accumulation at the walls. The ellipsoidal configuration space is thus responsible for the parallel alignment of a pusher, and must be taken into account. In comparison, we still observe a plateau for a puller, only without small peaks for perpendicular accumulation; a puller's shape plays a lesser role.

Note that, instead of a spherical swimmer, we used one that is very close to a sphere, to avoid numerical issues with the spherical swimmers sticking to the walls for very long times. The importance of accounting for shape is less pronounced for wider channels, since a swimmer experiences fewer steric wall interactions.
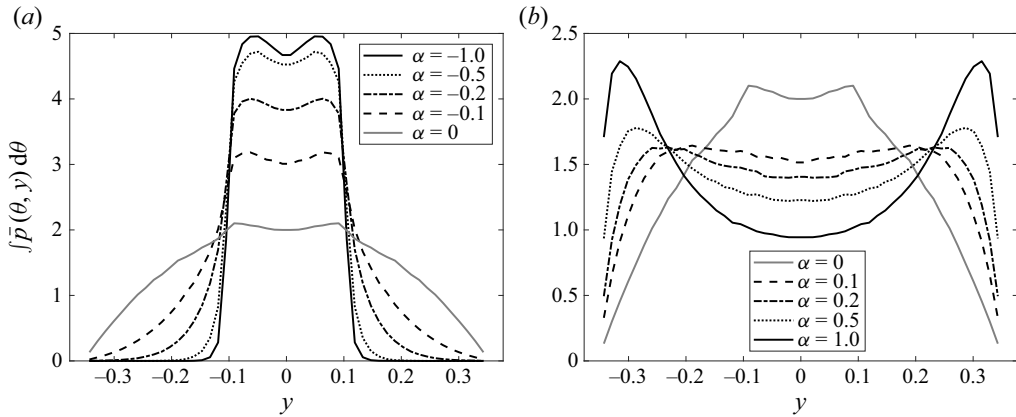
Figure 13. Cross-sectional invariant density $\int \bar{p}(\theta, y)\, d\theta$ with stresslet magnitude (*a*) $\alpha < 0$ (pullers); (*b*) $\alpha > 0$ (pushers). The channel has width $L = 1.2$ and the swimmer is an ellipsoid with $a = 2b = 0.5$, $X_{rot} = 0$, $U = 1$, $D_X = D_Y = 0.1$, $D_\theta = 0.01$, $\Gamma = 0.6$ in (8.1).
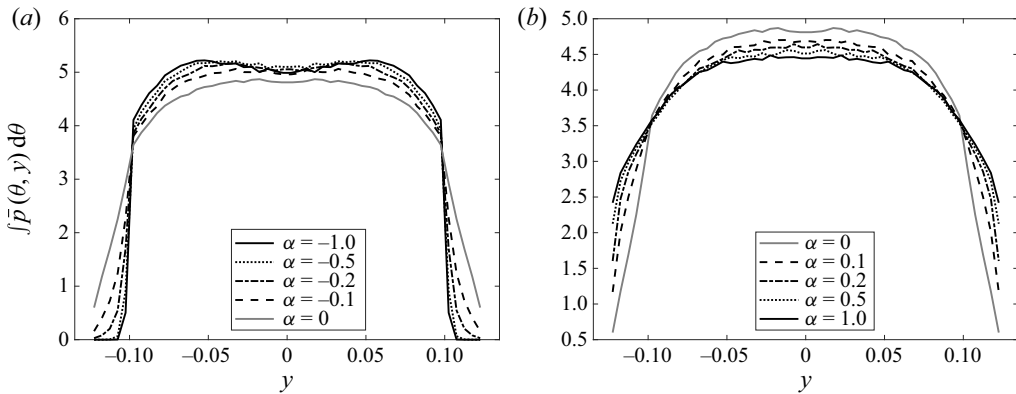

Figure 14. Cross-sectional invariant density for the same parameters as in figure 13, but with a configuration space corresponding to a nearly spherical swimmer with $a = 0.5$, $b = 0.475$. We keep $\Gamma = 0.6$ so that the hydrodynamic interactions are as in figure 13.

9. Discussion

We used both theory and numerics to analyse the dynamics of finite-sized swimmers in a channel. The shape of swimmers is embedded in their configuration space, which is defined even for non-smooth swimmers via their convex hull. Shape enters solely in the boundary conditions to the Fokker–Planck equation. Ignoring hydrodynamic interactions for simplicity, we derived a reduced equation in the small D_θ limit for both open and closed channels, from which we computed the invariant density. For open-channel geometry, we calculated the MRT. We used homogenization techniques and solved the cell problem to find the effective diffusivity. The shape of a swimmer is encoded in the rotational drift term μ in the reduced equation (4.17), and appears explicitly in the integral solution for the invariant density, MRT, and effective diffusivity. The integral of μ vanishes for a left–right-symmetric swimmer, and many of our expressions then greatly simplify. In particular the mean angular drift vanishes for such a symmetric swimmer. In § 8, we added hydrodynamic interactions with the walls and discussed the importance of shape.

We showed that, in a narrow channel, including the exact shape in configuration space is important for a pusher, but less so for a puller since they tend to be aligned perpendicular the walls.

A particular novelty in our work is to explicitly allow the position of the centre of rotation, X_{rot}, to vary. The sign of X_{rot} affects the configuration space, as shown in figure 4, and changes a swimmer's tendency to align with walls. When a swimmer's centre of rotation is behind its geometrical centre, it tends to align with a wall; in the opposite case, it tends to stay perpendicular to the wall even for a needle or circular swimmer (examples 5.1 and 5.2). A more systematic study of the role of X_{rot} for realistic swimmers will be the subject of future work.

In our work we focused on two-dimensional swimmers for simplicity and ease of presentation. However, generalizing the formalism to three-dimensional axisymmetric swimmers is straightforward (Nitsche & Brenner 1990). In that case, the wall distance function y_* is essentially the same as in two dimensions, and all that changes is that the ∂_θ^2 operator must be replaced by the three-dimensional surface Laplacian. The dynamics for three-dimensional axisymmetric swimmers will thus be similar to two-dimensional left–right-symmetric swimmers, with some quantitative changes. In particular, following almost the same calculations, we found the invariant density is given by a formula similar to (5.21), and when applied to spherical swimmers with $X_{rot} = 0$ it agrees with the results in Ezhilan & Saintillan (2015) and Elgeti & Gompper (2013). A Fully three-dimensional swimmer that is not axisymmetric will require considerably more work to implement: the configuration space has an extra dimension due to the extra degrees of freedom. Of course, this will potentially also make the dynamics richer, and will allow for interesting effects such as chirality.

Another challenging direction is to find asymptotic results when adding hydrodynamic interactions with boundaries. It is also possible to include variable swimmer shapes, which would allow the inclusion of flagella, by letting the configuration space itself be time dependent. Yet another potential avenue is to treat the interaction of multiple swimmers, in a manner analogous to Burada *et al.* (2009) and Bruna & Chapman (2013) for passive diffusing spheres.

Declaration of interests. The authors report no conflict of interest.

Author ORCIDs.

Ⓓ Hongfei Chen https://orcid.org/0000-0002-6476-4769;

Ⓓ Jean-Luc Thiffeault https://orcid.org/0000-0001-7724-7966.

Appendix A. Derivation of the MRT

In this appendix, we show how to from the reversal time formula (6.6) to the more explicit form (6.7) by eliminating the constant $\mathcal{C}$. First note that the numerator of (6.5) is

$$\int_{-\pi}^{\pi} \frac{\tilde{G}(\vartheta)}{\tilde{\mathcal{P}}(\vartheta)} \, \mathrm{d}\vartheta = \int_{-\pi}^{0} \frac{\tilde{G}(\vartheta)}{\tilde{\mathcal{P}}(\vartheta)} \, \mathrm{d}\vartheta + \int_{-\pi}^{0} \frac{\tilde{G}(\vartheta + \pi)}{\tilde{\mathcal{P}}(\vartheta + \pi)} \, \mathrm{d}\vartheta. \tag{A1}$$

We wish to relate $\tilde{\mathcal{P}}(\theta + \pi)$ to $\tilde{\mathcal{P}}(\theta) = \tilde{c}_1 \, w(\theta) \, \mathrm{e}^{\Phi(\theta)}$. We have $w(\theta + \pi) = w(\theta)$. The change in Φ over a period is, from (5.4),

$$\Phi(\theta + \pi) - \Phi(\theta) = \int_0^\pi \mu(\vartheta) \, \mathrm{d}\vartheta = \pi \bar{\mu}, \tag{A2}$$

since $\mu(\theta)$ is π-periodic. Here, $\bar{\mu}$ is the period-averaged $\mu(\theta)$ from (5.11); $\Phi(\theta)$ is only π-periodic when $\bar{\mu} = 0$, or equivalently $c_2 = 0$. It follows from (A2) that Φ must have the form

$$\Phi(\theta) = \bar{\mu} \, \theta + \tilde{\Phi}(\theta), \tag{A3}$$

where $\tilde{\Phi}(\theta)$ is π-periodic. We conclude from $\tilde{\mathcal{P}}(\theta) = \tilde{c}_1 \, w(\theta) \, \mathrm{e}^{\Phi(\theta)}$ that $\tilde{\mathcal{P}}(\theta + \pi) = \mathrm{e}^{\pi \bar{\mu}} \, \tilde{\mathcal{P}}(\theta)$. Similarly, for $-\pi \le \theta \le 0$,

$$
\begin{aligned}
\tilde{G}(\theta + \pi) &= \int_{-\pi}^{\theta + \pi} \tilde{\mathcal{P}}(\vartheta) \, \mathrm{d}\vartheta \\
&= \int_{-\pi}^0 \tilde{\mathcal{P}}(\vartheta) \, \mathrm{d}\vartheta + \int_0^{\theta + \pi} \tilde{\mathcal{P}}(\vartheta) \, \mathrm{d}\vartheta \\
&= \tilde{G}(0) + \mathrm{e}^{\pi \bar{\mu}} \, \tilde{G}(\theta).
\end{aligned} \tag{A4}
$$

Returning to (A1), we obtain

$$
\begin{aligned}
\int_{-\pi}^\pi \frac{\tilde{G}(\vartheta)}{\tilde{\mathcal{P}}(\vartheta)} \, \mathrm{d}\vartheta &= \int_{-\pi}^0 \frac{\tilde{G}(\vartheta)}{\tilde{\mathcal{P}}(\vartheta)} \, \mathrm{d}\vartheta + \int_{-\pi}^0 \frac{\tilde{G}(0) + \mathrm{e}^{\pi \bar{\mu}} \, \tilde{G}(\theta)}{\mathrm{e}^{\pi \bar{\mu}} \, \tilde{\mathcal{P}}(\vartheta)} \, \mathrm{d}\vartheta \\
&= 2 \int_{-\pi}^0 \frac{\tilde{G}(\vartheta)}{\tilde{\mathcal{P}}(\vartheta)} \, \mathrm{d}\vartheta + \tilde{G}(0) \, \mathrm{e}^{-\pi \bar{\mu}} \int_{-\pi}^0 \frac{\mathrm{d}\vartheta}{\tilde{\mathcal{P}}(\vartheta)}.
\end{aligned} \tag{A5}
$$

The denominator of $\mathcal{C}$ in (6.5) is

$$\int_{-\pi}^\pi \frac{\mathrm{d}\vartheta}{\tilde{\mathcal{P}}(\vartheta)} = \int_{-\pi}^0 \frac{\mathrm{d}\vartheta}{\tilde{\mathcal{P}}(\vartheta)} + \int_{-\pi}^0 \frac{\mathrm{d}\vartheta}{\tilde{\mathcal{P}}(\vartheta + \pi)} = (1 + \mathrm{e}^{-\pi \bar{\mu}}) \int_{-\pi}^0 \frac{\mathrm{d}\vartheta}{\tilde{\mathcal{P}}(\vartheta)}. \tag{A6}$$

Together, (A5) and (A6) give

$$\mathcal{C} \int_{-\pi}^0 \frac{\mathrm{d}\vartheta}{\tilde{\mathcal{P}}(\vartheta)} = \frac{1}{1 + \mathrm{e}^{-\pi \bar{\mu}}} \left(2 \int_{-\pi}^0 \frac{\tilde{G}(\vartheta)}{\tilde{\mathcal{P}}(\vartheta)} \, \mathrm{d}\vartheta + \tilde{G}(0) \, \mathrm{e}^{-\pi \bar{\mu}} \int_{-\pi}^0 \frac{\mathrm{d}\vartheta}{\tilde{\mathcal{P}}(\vartheta)} \right). \tag{A7}$$

We use this in the reversal time (6.6):

$$
\begin{aligned}
\tau_{rev} &= \mathcal{C} \int_{-\pi}^0 \frac{\mathrm{d}\vartheta}{\tilde{\mathcal{P}}(\vartheta)} - \int_{-\pi}^0 \frac{\tilde{G}(\vartheta)}{\tilde{\mathcal{P}}(\vartheta)} \, \mathrm{d}\vartheta \\
&= \frac{1}{1 + \mathrm{e}^{-\pi \bar{\mu}}} \left(2 \int_{-\pi}^0 \frac{\tilde{G}(\vartheta)}{\tilde{\mathcal{P}}(\vartheta)} \, \mathrm{d}\vartheta + \tilde{G}(0) \, \mathrm{e}^{-\pi \bar{\mu}} \int_{-\pi}^0 \frac{\mathrm{d}\vartheta}{\tilde{\mathcal{P}}(\vartheta)} \right) - \int_{-\pi}^0 \frac{\tilde{G}(\vartheta)}{\tilde{\mathcal{P}}(\vartheta)} \, \mathrm{d}\vartheta \\
&= \frac{1}{1 + \mathrm{e}^{-\pi \bar{\mu}}} \left(\tilde{G}(0) \, \mathrm{e}^{-\pi \bar{\mu}} \int_{-\pi}^0 \frac{\mathrm{d}\vartheta}{\tilde{\mathcal{P}}(\vartheta)} + (1 - \mathrm{e}^{-\pi \bar{\mu}}) \int_{-\pi}^0 \frac{\tilde{G}(\vartheta)}{\tilde{\mathcal{P}}(\vartheta)} \, \mathrm{d}\vartheta \right) \\
&= \frac{\tilde{G}(0) \, \mathrm{e}^{-\pi \bar{\mu}}}{1 + \mathrm{e}^{-\pi \bar{\mu}}} \int_{-\pi}^0 \frac{\mathrm{d}\vartheta}{\tilde{\mathcal{P}}(\vartheta)} + \frac{1 - \mathrm{e}^{-\pi \bar{\mu}}}{1 + \mathrm{e}^{-\pi \bar{\mu}}} \int_{-\pi}^0 \frac{\tilde{G}(\vartheta)}{\tilde{\mathcal{P}}(\vartheta)} \, \mathrm{d}\vartheta,
\end{aligned} \tag{A8}
$$

which is (6.7).

REFERENCES

AI, B., CHEN, Q., HE, Y., LI, F. & ZHENG, W. 2013 Rectification and diffusion of self-propelled particles in a two-dimensional corrugated channel. *Phys. Rev.* E **88**, 062129.

ALONSO-MATILLA, R., EZHILAN, B. & SAINTILLAN, D. 2016 Microfluidic rheology of active particle suspensions: kinetic theory. *Biomicrofluidics* **10**, 043505.

ALONSO-MATILLA, R. & SAINTILLAN, D. 2019 Interfacial instabilities in active viscous films. *J. Non-Newtonian Fluid Mech.* **259**, 57–64.

BEARON, R.N., HAZEL, A.L. & THORN, G.J. 2011 The spatial distribution of gyrotactic swimming micro-organisms in laminar flow fields. *J. Fluid Mech.* **680**, 602–635.

BECHINGER, C., DI LEONARDO, R., LÖWEN, H., REICHHARDT, C., VOLPE, G. & VOLPE, G. 2016 Active particles in complex and crowded environments. *Rev. Mod. Phys.* **88**, 045006.

BERKE, A.P., TURNER, L., BERG, H.C. & LAUGA, E. 2008 Hydrodynamic attraction of swimming microorganisms by surfaces. *Phys. Rev. Lett.* **101**, 038102.

BIANCHI, S., SAGLIMBENI, F. & DI LEONARDO, R. 2017 Holographic imaging reveals the mechanism of wall entrapment in swimming bacteria. *Phys. Rev.* X **7**, 011010.

BRICARD, A., CAUSSIN, J.-B., SAVOIE, D.D.C., CHIKKADI, V., SHITARA, K., CHEPIZHKO, O., PERUANI, F., SAINTILLAN, D. & BARTOLO, D. 2015 Emergent vortices in populations of confined colloidal rollers. *Nat. Commun.* **6**, 7470.

BRUNA, M. & CHAPMAN, S.J. 2013 Diffusion of finite-size particles in confined geometries. *Bull. Math. Biol.* **76** (4), 947–982.

BURADA, P.S., HÄNGGI, P., MARCHESONI, F., SCHMID, G. & TALKNER, P. 2009 Diffusion in confined geometries. *ChemPhysChem* **10** (1), 45–54.

CAPRINI, L. & MARCONI, U. 2018 Active particles under confinement and effective force generation among surfaces. *Soft Matt.* **14**, 9044–9054.

CATES, M.E. & TAILLEUR, J. 2013 When are active Brownian particles and run-and-tumble particles equivalent? Consequences for motility-induced phase separation. *Europhys. Lett.* **101**, 20010.

CHEN, Y., WANG, Z., CHU, K., CHEN, H., SHENG, Y. & TSAO, H. 2018 Hydrodynamic interaction induced breakdown of the state properties of active fluids. *Soft Matt.* **14**, 5319–5326.

CHILDRESS, S. & SOWARD, A.M. 1989 Scalar transport and alpha-effect for a family of cat's-eye flows. *J. Fluid Mech.* **205**, 99–133.

CHILUKURI, S., COLLINS, C.H. & UNDERHILL, P.T. 2014 Impact of external flow on the dynamics of swimming microorganisms near surfaces. *J. Phys.: Condens. Matter* **26**, 115101.

CONTINO, M., LUSHI, E., TUVAL, I., KANTSLER, V. & POLIN, M. 2015 Microalgae scatter off solid surfaces by hydrodynamic and contact forces. *Phys. Rev. Lett.* **115** (25), 258102.

COSTANZO, A., DI LEONARDO, R., RUOCCO, G. & ANGELANI, L. 2012 Transport of self-propelling bacteria in micro-channel flow. *J. Phys.: Condens. Matter* **24**, 065101.

CROWDY, D.G. & OR, Y. 2010 Two-dimensional point singularity model of a low-Reynolds-number swimmer near a wall. *Phys. Rev.* E **81**, 036313.

CROWDY, D.G. & SAMSON, O. 2011 Hydrodynamic bound states of a low-Reynolds-number swimmer near a gap in a wall. *J. Fluid Mech.* **667**, 309–335.

DADDI-MOUSSA-IDER, A., LISICKI, M., HOELL, C. & LÖWEN, H. 2018 Swimming trajectories of a three-sphere microswimmer near a wall. *J. Chem. Phys.* **148**, 134904.

DENISSENKO, P., KANSTLER, V., SMITH, D.J. & KIRKMAN-BROWN, J. 2012 Human spermatozoa migration in micro channels reveals boundary-following navigation. *Proc. Natl Acad. Sci. USA* **109**, 8007–8010.

DILUZIO, W.R., TURNER, L., MAYER, M., GARSTECKI, P., WEIBEL, D.B., BERG, H.C. & WHITESIDES, G.M. 2005 *Escherichia coli* swim on the right-hand side. *Nature* **435**, 1271–1274.

DRESCHER, K., DUNKEL, J., CISNEROS, L.H., GANGULY, S. & GOLDSTEIN, R.E. 2011 Fluid dynamics and noise in bacterial cell–cell and cell-surface scattering. *Proc. Natl Acad. Sci. USA* **108**, 10940–10945.

ELGETI, J. & GOMPPER, G. 2009 Self-propelled rods near surfaces. *Europhys. Lett.* **85**, 38002.

ELGETI, J. & GOMPPER, G. 2013 Wall accumulation of self-propelled spheres. *Europhys. Lett.* **101**, 48003.

ELGETI, J. & GOMPPER, G. 2015 Run-and-tumble dynamics of self-propelled particles in confinement. *Europhys. Lett.* **109**, 58003.

ELGETI, J. & GOMPPER, G. 2016 Microswimmers near surfaces. *Eur. Phys. J. Spec. Top.* **225**, 2333–2352.

EVANS, A.A. & LAUGA, E. 2010 Propulsion by passive filaments and active flagella near boundaries. *Phys. Rev.* E **82**, 041915.

EZHILAN, B., ALONSO-MATILLA, R. & SAINTILLAN, D. 2015 On the distribution and swim pressure of run-and-tumble particles in confinement. *J. Fluid Mech.* **781**, R4.

EZHILAN, B., PAHLAVAN, A.A. & SAINTILLAN, D. 2012 Chaotic dynamics and oxygen transport in thin films of aerotactic bacteria. *Phys. Fluids* **24**, 091701.

EZHILAN, B. & SAINTILLAN, D. 2015 Transport of a dilute active suspension in pressure-driven channel flow. *J. Fluid Mech.* **777**, 482–522.

FAUCI, L.J. & MCDONALD, A. 1995 Sperm motility in the presence of boundaries. *Bull. Math. Biol.* **57**, 679–699.

FRYMIER, P.D., FORD, R.M., BERG, H.C. & CUMMINGS, P.T. 1995 Three-dimensional tracking of motile bacteria near a solid planar surface. *Proc. Natl Acad. Sci. USA* **92**, 6195–6199.

GACHELIN, J., MIÑO, G., BERTHET, H., LINDNER, A., ROUSSELET, A. & CLÉMENT, É. 2013 Non-newtonian viscosity of *Escherichia coli* suspensions. *Phys. Rev. Lett.* **110**, 268103.

GREBENKOV, D.S. 2016 Universal formula for the mean first passage time in planar domains. *Phys. Rev. Lett.* **117**, 260201.

HAPPEL, J. & BRENNER, H. 1983 *Low Reynolds Number Hydrodynamics*. Martinus Nijhoff (Kluwer).

HERNANDEZ-ORTIZ, J.P., STOLTZ, C.G. & GRAHAM, M.D. 2005 Transport and collective dynamics in suspensions of confined swimming particles. *Phys. Rev. Lett.* **95**, 204501.

HERNANDEZ-ORTIZ, J.P., UNDERHILL, P.T. & GRAHAM, M.D. 2009 Dynamics of confined suspensions of swimming particles. *J. Phys.: Condens. Matter* **21**, 204107.

HILL, J., KALKANCI, O., MCMURRY, J.L. & KOSER, H. 2007 Hydrodynamic surface interactions enablei *Escherichia coli* to seek efficient routes to swim upstream. *Phys. Rev. Lett.* **98**, 068101.

HOLCMAN, D. & SCHUSS, Z. 2014 The narrow escape problem. *SIAM Rev.* **56** (2), 213–257.

KAISER, A., WENSINK, H.H. & LÖWEN, H. 2012 How to capture active particles. *Phys. Rev. Lett.* **108**, 268307.

KANTSLER, V., DUNKEL, J., POLIN, M. & GOLDSTEIN, R.E. 2013 Ciliary contact interactions dominate surface scattering of swimming eukaryotes. *Proc. Natl Acad. Sci. USA* **110** (4), 1187–1192.

KATZ, D.F. 1974 Propulsion of microorganisms near solid boundaries. *J. Fluid Mech.* **64**, 33–49.

KATZ, D.F. & BLAKE, J.R. 1975 flagellar motions near walls. *Swimming Flying Nat.* **1**, 173–184.

KATZ, D.F., BLAKE, J.R. & PAVERIFONTANA, S.L. 1975 On the movement of slender bodies near plane boundaries at low Reynolds number. *J. Fluid Mech.* **72**, 529–540.

KAYNAN, U. & YARIV, E. 2017 Stokes resistance of a cylinder near a slippery wall. *Phys. Rev. Fluids* **2**, 104103.

KIM, M.Y., DRESCHER, K., PARK, O.S., BASSLER, B. & STONE, H.A. 2014 Filaments in curved streamlines: rapid formation of *Staphylococcus aureus* biofilm streamers. *New J. Phys.* **16**, 065024.

KOUMAKIS, N., MAGGI, C. & DI LEONARDO, R. 2014 Directed transport of active particles over asymmetric energy barriers. *Soft Matt.* **10**, 5695–5701.

KROCHAK, P.J., OLSON, J.A. & MARTINEZ, D.M. 2010 Near-wall estimates of the concentration and orientation distribution of a semi-dilute rigid fibre suspension in Poiseuille flow. *J. Fluid Mech.* **653**, 431–462.

KURELLA, V., TZOU, J.C., COOMBS, D. & WARD, M.J. 2015 Asymptotic analysis of first passage time problems inspired by ecology. *Bull. Math. Biol.* **77** (1), 83–125.

KURZTHALER, C. & FRANOSCH, T. 2017 Intermediate scattering function of an anisotropic Brownian circle swimmer. *Soft Matt.* **13**, 6396–6406.

KURZTHALER, C., LEITMANN, S. & FRANOSCH, T. 2016 Intermediate scattering function of an anisotropic active Brownian particle. *Sci. Rep.* **6**, 36702.

LAMBERT, G., LIAO, D. & AUSTIN, R.H. 2010 Collective escape of chemotactic swimmers through microscopic ratchets. *Phys. Rev. Lett.* **104**, 168102.

LAUGA, E. 2006 Swimming in circles: motion of bacteria near solid boundaries. *Biophys. J.* **90**, 400–412.

LAUGA, E. & POWERS, T.R. 2009 The hydrodynamics of swimming microorganisms. *Rep. Prog. Phys.* **72**, 096601.

LEE, C.F. 2013 Active particles under confinement: aggregation at the wall and gradient formation inside a channel. *New J. Phys.* **15**, 055007.

LEE, M., SZUTTOR, K. & HOLM, C. 2019 A computational model for bacterial run-and-tumble motion. *J. Chem. Phys.* **17**, 174111.

LEFAUVE, A. & SAINTILLAN, D. 2014 Globally aligned states and hydrodynamic traffic jams in confined suspensions of active asymmetric particles. *Phys. Rev. E* **89**, 021002.

LI, G., BENSSON, J., NISIMOVA, L., MUNGER, D., MAHAUTMR, P., TANG, J.X., MAXEY, M.R. & BRUN, Y.V. 2011 Accumulation of swimming bacteria near a solid surface. *Phys. Rev. E* **84**, 041932.

LI, G., TAM, L. & TANF, J. 2008 Amplified effect of Brownian motion in bacterial near-surface swimming. *Proc. Natl Acad. Sci. USA* **105**, 18355–18359.

LI, G. & TANG, J.X. 2009 Accumulation of microswimmers near a surface mediated by collision and rotational Brownian motion. *Phys. Rev. Lett.* **103**, 078101.

LI, G.-J. & ARDEKANI, A.M. 2014 Hydrodynamic interaction of microswimmers near a wall. *Phys. Rev.* E **90**, 013010.

LOPEZ, D. & LAUGA, E. 2014 Dynamics of swimming bacteria at complex interfaces. *Phys. Fluids* **26**, 071902.

LUSHI, E. 2016 Stability and dynamics of anisotropically-tumbling chemotactic swimmers. *Phys. Rev.* E **94**, 022414.

LUSHI, E., GOLDSTEIN, R.E. & SHELLEY, M.J. 2012 Collective chemotactic dynamics in the presence of self-generated fluid flows. *Phys. Rev.* E **86**, 040902.

LUSHI, E., GOLDSTEIN, R.E. & SHELLEY, M.J. 2018 Nonlinear concentration patterns and bands in autochemotactic suspensions. *Phys. Rev.* E **98**, 052411.

LUSHI, E., KANTSLER, V. & GOLDSTEIN, R.E. 2017 Scattering of biflagellate microswimmers from surfaces. *Phys. Rev.* E **96** (2), 023102.

LUSHI, E. & VLAHOVSKA, P.M. 2015 Periodic and chaotic orbits of plane-confined micro-rotors in creeping flows. *J. Nonlinear Sci. Appl.* **25**, 1111–1123.

LUSHI, E., WIOLAND, H. & GOLDSTEIN, R.E. 2014 Fluid flows created by swimming bacteria drive self-organization in confined suspensions. *Proc. Natl Acad. Sci. USA* **111** (27), 9733–9738.

MAJDA, A.J. & KRAMER, P.R. 1999 Simplified models for turbulent diffusion: theory, numerical modelling and physical phenomena. *Phys. Rep.* **314** (4–5), 237–574.

MALGARETTI, P. & STARK, H. 2017 Model microswimmers in channels with varying cross section. *J. Chem. Phys.* **146**, 174901.

MARCHETTI, M.C., JOANNY, J.F., RAMASWAMY, S., LIVERPOOL, T.B., PROST, J., RAO, M. & SIMHA, R.A. 2013 Hydrodynamics of soft active matter. *Rev. Mod. Phys.* **85**, 1143–1189.

MARCOTTE, F., DOERING, C.R., THIFFEAULT, J.-L & YOUNG, W.R. 2018 Optimal heat transfer and optimal exit times. *SIAM J. Appl. Maths* **78** (1), 591–608.

MARTENS, K., ANGELANI, L., DI LEONARDO, R. & BOCQUET, L. 2012 Probability distributions for the run-and-tumble bacterial dynamics: an analogy to the Lorentz model. *Europhys. Lett.* **35**, 1–6.

MATHIJSSEN, A.J.T.M., DOOSTMOHAMMADI, A., YEOMANS, J.M. & SHENDRUK, T.N. 2016 Hotspots of boundary accumulation: dynamics and statistics of microswimmers in flowing films. *J. R. Soc. Interface* **13**, 20150936.

MCCARTY, P. & HORSTHEMKE, W. 1988 Effective diffusion for steady two-dimensional flow. *Phys. Rev.* A **37** (6), 2112–2117.

MIRZAKHANLOO, M. & ALAM, M.-R. 2018 Flow characteristics of *Chlamydomonas* result in purely hydrodynamic scattering. *Phys. Rev.* E **98** (1), 012603.

MOK, R., DUNKEL, J. & KANTSLER, V. 2019 Geometric control of bacterial surface accumulation. *Phys. Rev.* E **99**, 052607.

MOLAEI, M., BARRY, M., STOCKER, R. & SHENG, J. 2014 Failed escape: solid surfaces prevent tumbling of *Escherichia coli*. *Phys. Rev. Lett.* **113**, 068103.

NASH, R.W., ADHIKARI, R., TAILLEUR, J. & CATES, M.E. 2010 Run-and-tumble particles with hydrodynamics: sedimentation, trapping, and upstream swimming. *Phys. Rev. Lett.* **104**, 258101.

NIKOLA, N., SOLON, A.P., KAFRI, Y., KARDAR, M., TAILLEUR, J. & VOITURIEZ, R. 2016 Active particles with soft and curved walls: equation of state, ratchets, and instabilities. *Phys. Rev. Lett.* **117**, 098001.

NITSCHE, J.M. & BRENNER, H. 1990 On the formulation of boundary conditions for rigid non spherical Brownian particles near solid walls: applications to orientation-specific reactions with immobilized enzymes. *J. Colloid Interface Sci.* **138**, 21–41.

OBUSE, K. & THIFFEAULT, J.-L. 2012 A low-Reynolds-number treadmilling swimmer near a semi-infinite wall. In *IMA Volume on Natural Locomotion in Fluids and on Surfaces: Swimming, Flying, and Sliding* (ed. S. Childress, A. Hosoi, W.W. Schultz & J. Wang), pp. 197–206. Springer.

PAKSA, A., *et al.* 2016 Repulsive cues combined with physical barriers and cell–cell adhesion determine progenitor cell positioning during organogenesis. *Nat. Commun.* **7**, 11288.

PAVLIOTIS, G.A. 2014 *Stochastic Processes and Applications*. Springer.

RAZIN, N., VOITURIEZ, R., ELGETI, J. & GOV, N.S. 2017 Generalized Archimedes' principle in active fluids. *Phys. Rev.* E **96**, 032606.

REDNER, G.S., HAGAN, M.F. & BASKARAN, A. 2013 Structure and dynamics of a phase-separating active colloidal fluid. *Phys. Rev. Lett.* **110**, 055701.

REDNER, S. 2001 *A Guide to First-Passage Processes*. Cambridge University Press.

ROTHSCHILD, L. 1963 Non-random distribution of bull spermatozoa in a drop of sperm suspension. *Nature* **198**, 1221–1222.

RUSCONI, R., LECUYER, S., GUGLIELMINI, L. & STONE, H.A. 2010 Laminar flow around corners triggers the formation of biofilm streamers. *J. R. Soc. Interface* **7**, 1293–1299.

SAGUES, F. & HORSTHEMKE, W. 1986 Diffusive transport in spatially periodic hydrodynamic flows. *Phys. Rev.* A **34** (5), 4136–4143.

SAINTILLAN, D. 2010 The dilute rheology of swimming suspensions: a simple kinetic model. *Expl Mech.* **50**, 1275–1281.

SAINTILLAN, D., SHAQFEH, E.S.G. & DARVE, E. 2006a Effect of flexibility on the shear-induced migration of short-chain polymers in parabolic channel flow. *J. Fluid Mech.* **557**, 297–306.

SAINTILLAN, D., SHAQFEH, E.S.G. & DARVE, E. 2006b The growth of concentration fluctuations in dilute dispersions of orientable and deformable particles under sedimentation. *J. Fluid Mech.* **553**, 347–388.

SAINTILLAN, D. & SHELLEY, M.J. 2007 Orientational order and instabilities in suspensions of self-locomoting rods. *Phys. Rev. Lett.* **99**, 058102.

SAINTILLAN, D. & SHELLEY, M.J. 2008 Instabilities and pattern formation in active particle suspensions: kinetic theory and continuum simulations. *Phys. Rev. Lett.* **100**, 178103.

SAINTILLAN, D. & SHELLEY, M.J. 2011 Emergence of coherent structures and large-scale flows in motile suspensions. *J. R. Soc. Interface* **9**, 571–585.

SAINTILLAN, D. & SHELLEY, M.J. 2013 Active suspensions and their nonlinear models. *C. R. Phys.* **14**, 497–517.

SCHAAR, K., ZÖTTL, A. & STARK, H. 2015 Detention times of microswimmers close to surfaces: influence of hydrodynamic interactions and noise. *Phys. Rev. Lett.* **115** (3), 038101.

SEPÚLVEDA, N. & SOTO, R. 2017 Wetting transitions displayed by persistent active particles. *Phys. Rev. Lett.* **119**, 078001.

SEPÚLVEDA, N. & SOTO, R. 2018 Universality of active wetting transitions. *Phys. Rev.* E **98**, 052141.

SHUM, H., GAFFNEY, E. & SMITH, D. 2010 Modelling bacterial behaviour close to a no-slip plane boundary: the influence of bacterial geometry. *Proc. R. Soc.* A **466**, 1725–1748.

SIPOS, O., NAGY, K., DI LEONARDO, R. & GALAJDA, P. 2015 Hydrodynamic trapping of swimming bacteria by convex walls. *Phys. Rev. Lett.* **114**, 258104.

SOLON, A.P., FILY, Y., BASKARAN, A., CATES, M.E., KAFRI, Y., KARDAR, M. & TAILLEUR, J. 2015 Pressure is not a state function for generic active fluids. *Nat. Phys.* **11**, 673–678.

SPAGNOLIE, S.E. & LAUGA, E. 2012 Hydrodynamics of self-propulsion near boundaries: predictions and accuracy of far-field approximations. *J. Fluid Mech.* **700**, 105–147.

SPAGNOLIE, S.E., MORENO-FLORES, G.R., BARTOLO, D. & LAUGA, E. 2015 Geometric capture and escape of a microswimmer colliding with an obstacle. *Soft Matt.* **11**, 3396–3411.

SPECK, T. 2020 Collective forces in scalar active matter. *Soft Matt.* **16**, 2652–2663.

STENHAMMAR, J., MARENDUZZO, D., ALLEN, R.J. & CATES, M.E. 2014 Phase behaviour of active Brownian particles: the role of dimensionality. *Soft Matt.* **10**, 1489–1499.

SWAN, J.W. & BRADY, J.F. 2007 Simulation of hydrodynamically interacting particles near a no-slip boundary. *Phys. Fluids* **19**, 113306.

TAILLEUR, J. & CATES, M.E. 2009 Sedimentation, trapping, and rectification of dilute bacteria. *Europhys. Lett.* **86**, 60002.

TAKAGI, D., PALACCI, J., BRAUNSCHWEIG, A., SHELLEY, M. & ZHANG, J. 2014 Hydrodynamic capture of microswimmers into sphere-bound orbits. *Soft Matt.* **10**, 1784–1789.

TAKATORI, S.C., YAN, W. & BRADY, J.F. 2014 Swim pressure: stress generation in active matter. *Phys. Rev. Lett.* **113**, 028103.

VAN TEEFFELEN, S. & LÖWEN, H. 2008 Dynamics of a Brownian circle swimmer. *Phys. Rev.* E **78**, 020101.

TEN HAGEN, B., WITTKOWSKI, R. & LÖWEN, H. 2011 Brownian dynamics of a self-propelled particle in shear flow. *Phys. Rev.* E **84**, 031105.

TEN HAGEN, B., WITTKOWSKI, R., TAKAGI, D., KÜMMEL, F., BECHINGER, C. & LÖWEN, H. 2015 Can the self-propulsion of anisotropic microswimmers be described by using forces and torques. *J. Phys.: Condens. Matter* **27**, 194110.

THEERS, M., WESTPHAL, E., QI, K., WINKLER, R.G. & GOMPPER, G. 2018 Clustering of microswimmers: interplay of shape and hydrodynamics. *Soft Matt.* **14**, 8590–8603.

THEILLARD, M., MATILLA, R.A. & SAINTILLAN, D. 2017 Geometric control of active collective motion. *Soft Matt.* **13**, 363–375.

TIAN, W., GU, Y., GUO, Y. & CHEN, K. 2017 Anomalous boundary deformation induced by enclosed active particles. *Chin. Phys.* B **26**, 100502.

VOLPE, G., BUTTINONI, I., VOGT, D., KÜMMERER, H.J. & BECHINGER, C. 2011 Microswimmers in patterned environments. *Soft Matt.* **7**, 8810–8815.

VOLPE, G., GIGAN, S. & VOLPE, G. 2014 Simulation of the active Brownian motion of a microswimmer. *Am. J. Phys.* **82** (7), 659–664.

WAGNER, C., HAGAN, M. & BASKARAN, A. 2019 Response of active Brownian particles to boundary driving. *Phys. Rev.* E **100**, 042610.

WAGNER, C., HAGAN, M.F. & BASKARAN, A. 2017 Steady-state distributions of ideal active Brownian particles under confinement and forcing. *J. Stat. Mech.* **4** (4), 043203.

WARD, M.J. & KELLER, J.B. 1993 Strong localized perturbations of eigenvalue problems. *SIAM J. Appl. Maths* **53** (3), 770–798.

WENSINK, H.H. & LÖWEN, H. 2008 Aggregation of self-propelled colloidal rods near confining walls. *Phys. Rev.* E **78**, 031409.

WIOLAND, H., LUSHI, E. & GOLDSTEIN, R.E. 2016 Directed collective motion of bacteria under channel confinement. *New J. Phys.* **18**, 081001.

WOOLLEY, D.M. 2003 Motility of spermatozoa at surfaces. *Reproduction* **126**, 259–270.

YAN, W. & BRADY, J.F. 2015 The force on a boundary in active matter. *J. Fluid Mech.* **785**, R1.

YARIV, E. & SCHNITZER, O. 2014 Ratcheting of Brownian swimmers in periodically corrugated channels: a reduced Fokker–Planck approach. *Phys. Rev.* E **90**, 032115.

YEO, K., LUSHI, E. & VLAHOVSKA, P.M. 2015 Collective dynamics in a binary mixture of hydrodynamically coupled micro-rotors. *Phys. Rev. Lett.* **114**, 188301.

ZARGAR, R., NAJAFI, A. & MIRI, M. 2009 Three-sphere low-Reynolds-number swimmer near a wall. *Phys. Rev.* E **80**, 026308.

ZÖTTL, A. & STARK, H. 2016 Emergent behavior in active colloids. *J. Phys.: Condens. Matter* **28**, 253001.